

1 **Ammonia emissions and depositions over the contiguous United States derived**
2 **from IASI and CrIS using the directional derivative approach**

3 Zitong Li^{1,2}, Kang Sun^{3,4*}, Kaiyu Guan^{1,2,5,6*}, Sheng Wang^{1,2}, Bin Peng^{1,2,5,7}, Lieven Clarisse⁸,
4 Martin Van Damme^{8,9}, Pierre-François Coheur⁹, Karen Cady-Pereira¹⁰, Mark W. Shephard¹¹,
5 Mark Zondlo¹², Daniel Moore¹²

6 ¹Agroecosystem Sustainability Center, Institute for Sustainability, Energy, and Environment,
7 University of Illinois Urbana-Champaign, Urbana, IL, USA.

8 ²Department of Natural Resources and Environmental Sciences, College of Agricultural,
9 Consumer and Environmental Sciences, University of Illinois Urbana-Champaign, Urbana, IL,
10 USA.

11 ³Department of Civil, Structural and Environmental Engineering, University at Buffalo, Buffalo,
12 NY, USA.

13 ⁴Research and Education in Energy, Environment and Water Institute, University at Buffalo,
14 Buffalo, NY, USA.

15 ⁵National Center for Supercomputing Applications, University of Illinois Urbana-Champaign,
16 Urbana, IL, USA.

17 ⁶Department of Computer Science, University of Illinois Urbana-Champaign, Urbana, IL, USA.

18 ⁷Department of Crop Sciences, University of Illinois Urbana-Champaign, Urbana, IL, USA.

19 ⁸Université libre de Bruxelles (ULB), BLU-ULB research Center, Spectroscopy, Quantum
20 Chemistry and Atmospheric Remote Sensing (SQUARES), Brussels, Belgium

21 ⁹Royal Belgian Institute for Space Aeronomy (BIRA-IASB), Brussels, Belgium.

22 ¹⁰Atmospheric and Environmental Research, Lexington, MA, USA.

23 ¹¹Environment and Climate Change Canada, Toronto, ON, Canada.

24 ¹²Department of Civil and Environmental Engineering, Princeton University, Princeton, NJ,
25 USA.

26 Corresponding authors: Kang Sun (kangsun@buffalo.edu), Kaiyu Guan (kaiyug@illinois.edu)

27

28 **Abstract**

29 Atmospheric ammonia (NH₃), primarily emitted from agriculture, poses
30 significant threats to ecosystems, climate, and human health through nitrogen
31 deposition and secondary aerosol formation. NH₃ flux estimates remain highly
32 uncertain due to limited direct observations and complex emission–deposition
33 processes. Here, we estimated NH₃ fluxes over the contiguous United States using
34 satellite observations from the Infrared Atmospheric Sounding Interferometer (IASI,
35 2008–2022) and Cross-track Infrared Sounder (CrIS, 2012–2022) by applying a
36 directional derivative approach. Our results highlight major agricultural emission
37 hotspots, including the San Joaquin Valley in California, the Snake River Valley in
38 Idaho, the Texas panhandle, the Great Plains, Southeastern Pennsylvania, and
39 Eastern North Carolina. NH₃ removal is predominantly driven by deposition near

40 source areas rather than chemical transformation, with strong sinks in vegetation-
41 dense regions such as forests, grasslands, shrublands, and wetlands. Seasonal flux
42 variations show peaks in warm months and lower values in winter, driven by
43 temperature-dependent volatilization from livestock production and fertilizer
44 application. Compared with bottom-up inventory, satellite-based estimates capture
45 general spatial and seasonal patterns, while also revealing additional insights into key
46 flux hotspots and peak periods. CrIS consistently reports higher fluxes than IASI,
47 especially in spring, reflecting differences in their overpass times. Combining IASI
48 (morning overpass) and CrIS (midday overpass) observations enables a better
49 understanding of diurnal NH₃ flux dynamics. These findings provide critical insights
50 into NH₃ spatiotemporal variabilities, complementing inventory-based approaches and
51 informing nitrogen management and environmental policy, particularly in regions with
52 limited ground-based monitoring.

53 **1. Introduction**

54 Atmospheric NH₃ is the most abundant alkaline gas (Asman et al., 1998; Sutton
55 et al., 2020), and a major component of reactive nitrogen (Galloway et al., 2004). It is
56 removed primarily through two pathways: deposition and chemical transformation.
57 Deposition occurs when atmospheric NH₃ is taken up by surfaces via dry or wet
58 processes near its emission sources. Chemical removal involves reactions with sulfuric,
59 nitric, and hydrochloric acids (Loubet et al., 2009), forming particulate ammonium
60 (NH₄⁺) and secondary pollutants (Behera and Sharma, 2010; Wang et al., 2015).
61 Global NH₃ emissions have more than doubled since pre-industrial times (Galloway et
62 al., 2003), driving a cascade of environmental consequences. NH₃ deposition and its
63 secondary chemical products contribute to ecosystem eutrophication and soil
64 acidification, disrupting natural nutrient cycles and reducing biodiversity (van Breemen
65 et al., 1982; Heil and Diemont, 1983; Sutton et al., 2008). These processes degrade
66 air quality, threaten human health (Ma et al., 2021), and influence climate through
67 radiative forcing alterations (Erisman et al., 2013; Gong et al., 2024).

68 NH₃ is emitted from various sources, including domestic animals (40%),
69 synthetic fertilizers (17%), biomass burning (11%), natural sources (19%), crops (7%)
70 and humans and pets (5%) (Bouwman et al., 1997). However, large-scale ground-
71 based measurements of NH₃ emissions are sparse due to the challenges associated
72 with accurately capturing gaseous NH₃. Observations of NH₃ fluxes are further
73 constrained by its sharp spatial gradients and short tropospheric lifetime, typically less
74 than 24 hours (Adams et al., 2019; Wang et al., 2023). Regional and global NH₃ fluxes
75 are often estimated using bottom-up approaches that rely on emission factors and
76 spatial allocation of NH₃-emitting activities (Liu et al., 2022). However, these estimates
77 have large uncertainties, reaching up to 50% (Bouwman et al., 1997). A major source
78 of uncertainty is the lack of reliable statistics on fertilizer use and animal waste
79 production. Regional variations in agricultural practices complicate scaling local
80 observations to global estimates (Luo et al., 2022). Further challenges arise from
81 limited understanding of emissions from natural sources and biomass burning

82 (Dentener and Crutzen, 1994) and the dependence of NH₃ volatilization on
83 environmental conditions (Sommer et al., 1991).

84 Advances in satellite-based atmospheric retrievals have introduced powerful
85 tools for estimating trace gas fluxes, enabling large-scale investigation of gas
86 dynamics. For example, the Infrared Atmospheric Sounding Interferometer (IASI) and
87 the Cross-track Infrared Sounder (CrIS) have identified large NH₃ point sources
88 worldwide that were absent from bottom-up inventories (Van Damme et al., 2018;
89 Dammers et al., 2019). Chemical transport models (CTMs) have been widely
90 employed to derive gas fluxes from satellite observations (Cao et al., 2020, 2022; Chen
91 et al., 2021; Marais et al., 2021). However, the computational demands of running
92 CTMs at fine temporal and spatial scales pose significant limitations to fully leverage
93 the coverage and resolutions of new-generation satellite products. To complement
94 CTMs, observational-data-driven approaches have been developed to derive gas
95 emissions directly from satellite Level 2 products. The flux divergence method, for
96 example, has been used to estimate NO_x fluxes (Beirle et al., 2019, 2021). Closely
97 related to the flux divergence method, the directional derivative approach (DDA)
98 estimates fluxes with additional agility (Ayazpour et al., 2025; Sun, 2022) and
99 demonstrates broad applicability across various atmospheric species and regions
100 (Lonsdale and Sun, 2023).

101 In this study, we applied the DDA to estimate NH₃ fluxes across the contiguous
102 United States (CONUS). We derived top-down NH₃ fluxes at 0.1° resolution using
103 observations from two space-based instruments: the Infrared Atmospheric Sounding
104 Interferometer (IASI) and the Cross-track Infrared Sounder (CrIS). This study
105 addresses the following questions: 1) How accurately can satellite observations from
106 IASI and CrIS be used to estimate NH₃ fluxes? 2) What are the spatiotemporal patterns
107 of NH₃ fluxes over the CONUS? Our findings aim to enhance the understanding of
108 reactive nitrogen cycling and provide valuable information for environmental and policy
109 applications.

110 **2. Data and Methods**

111 **2.1 Data**

112 IASI and CrIS datasets use distinct retrieval approaches, providing two
113 independent datasets and complementary perspectives for analyzing NH₃ flux patterns.
114 IASI onboard the Metop-A/B/C meteorological payload was launched by the European
115 Organisation for the Exploitation of Meteorological Satellites (EUMETSAT). Operating
116 in a polar orbit, IASI provides global coverage with two overpass times daily, morning
117 (09:30 local solar time, LST) and at night (21:30 LST). The instrument features a
118 circular footprint on ground of 12 km along the satellite track and a swath width of 2200
119 km ($\pm 48.3^\circ$) (Clerbaux et al., 2009). IASI measurements generate vertical column
120 densities (VCDs) of NH₃ using machine learning-based retrieval algorithms. We
121 utilized daytime (09:30 LST) NH₃ VCD measurements over the CONUS from January
122 2008 to December 2022. The data was sourced from the Level 2 reanalysis product of
123 the ANNI-NH₃-v4R dataset (Clarisse et al., 2023) from Metop-A (January 2008 to

124 October 2021), Metop-B (March 2013 to December 2022) and Metop-C (September
125 2019 to December 2022). Additionally, we excluded Metop-A data after 2019 due to a
126 drift in Metop-A's overpass time towards the end of its operational life. CrIS is onboard
127 the Suomi-NPP, NOAA-20 and NOAA-21 satellites. It also operates in a polar orbit
128 with two overpass times daily, early afternoon (13:30 LST) and after midnight (01:30
129 LST). CrIS features a swath width identical to IASI (2200 km) and a similar ground
130 pixel resolution (14 km circular pixels at nadir). NH₃ VCDs are generated using the fast
131 physical retrieval (CFPR) approach (Shephard and Cady-Pereira, 2015; Shephard et
132 al., 2020). We used daytime (13:30 LST) NH₃ VCDs measured by CrIS-NPP (June
133 2012 to May 2021) and CrIS-NOAA-20 (March 2019 to December 2022) over the
134 CONUS for the period from June 2012 to December 2022. The dataset was derived
135 from the Level 2 CrIS NH₃ version 1.6.4 product.

136 We used gridded monthly NH₃ emission inventories from the Harmonized
137 Emissions Component (HEMCO) 3.0 for 2016 with a spatial resolution of 0.1° (Lin et
138 al., 2021). HEMCO converts publicly available emissions data, such as SMOKE
139 outputs, into inputs compatible with atmospheric models like GEOS-Chem. The
140 inventory integrates data from the National Emissions Inventory and includes key NH₃
141 sources such as agriculture, industry, and natural emissions. We use this bottom-up
142 inventory from HEMCO to compare with satellite-derived fluxes, providing insights into
143 their consistency and helping to assess the utility of satellite-based estimates.

144 We also incorporated additional datasets to support NH₃ flux estimation and
145 analysis. Hourly horizontal wind data at 100 and 10 m above the surface was utilized
146 to estimate NH₃ fluxes from satellite observations. The data was obtained from the
147 ERA5 reanalysis at a spatial resolution of 0.25° (Hersbach et al., 2020) spanning 2008
148 to 2022. The 2021 release of the National Land Cover Database (NLCD) with a
149 resolution of 30 meters was used to analyze the spatial patterns of NH₃ fluxes across
150 different land cover types. Land and water mask data from the North American Land
151 Data Assimilation System (NLDAS) unified mask were used to exclude water body
152 data due to the larger noise of the satellite retrievals over these areas.

153 **2.2 NH₃ flux estimations**

154 **2.2.1 Directional derivative approach (DDA)**

155 The estimation of emissions (E) from satellite-observed VCDs (Ω) is grounded
156 in the principle of mass conservation as in Eq. 1, which is in the same form as
157 presented in the previous DDA literature (Sun, 2022; Ayazpour et al., 2025). DDA
158 accounts for horizontal transport, topographic effects, and chemical transformation
159 influencing gas distribution. Three estimators within the DDA framework are labeled in
160 Eq. 1 as DD , DD_{topo} , and DD_{chem} , representing the directional derivative of column
161 densities, the directional derivative with consideration of topography, and the
162 directional derivative with consideration of both topography and chemistry. The DD
163 estimator ($\vec{u} \cdot (\nabla \Omega)$) captures the horizontal advection of NH₃, representing the
164 directional derivatives of the VCDs with respect to horizontal wind vectors representing
165 the planetary boundary layer (\vec{u} , 100 m winds). $\nabla = (\partial/\partial x, \partial/\partial y)$ is the horizontal

166 vector differential operator. Ayazpour et al. (2025) evaluated DD estimators calculated
 167 using column amounts and winds at a range of altitudes in an atmospheric model with
 168 the model-ingested emission and found that winds from 100-800 m give similar and
 169 consistent results. We choose 100 m wind because it has been widely used in previous
 170 studies (Goldberg et al., 2022; Lonsdale and Sun, 2023) and is readily available from
 171 the ERA5 single-level product. The DD_{topo} estimator accounts for the topography
 172 term ($X\Omega\vec{u}_0 \cdot (\nabla z_0)$), which is driven by the directional derivatives of the surface
 173 altitudes (z_0 , obtained from Level 2 satellite data) relative to near-surface wind vectors
 174 (\vec{u}_0 , 10 m winds). This component captures the influence of terrain on NH_3 movement.
 175 For example, variations in elevation can create localized gradients that resemble NH_3
 176 fluxes. The DD_{chem} estimator considers the chemistry term ($k\Omega$), representing
 177 chemical interactions between NH_3 and atmospheric acids which result in the
 178 formation of particulate matter.

$$\begin{aligned}
 179 \quad & \langle E \rangle = \underbrace{\langle \vec{u} \cdot (\nabla \Omega) \rangle}_{DD} + \overbrace{X \langle \Omega \vec{u}_0 \cdot (\nabla z_0) \rangle + k \langle \Omega \rangle}^{DD_{topo}} + \underbrace{\phantom{X \langle \Omega \vec{u}_0 \cdot (\nabla z_0) \rangle + k \langle \Omega \rangle}}_{DD_{chem}} \quad (1) \\
 180 \quad & \\
 181 \quad &
 \end{aligned}$$

182 Here $\langle \rangle$ denotes the spatiotemporal averaging operator already implemented in
 183 the physical oversampling framework (Sun et al., 2018). This method leverages the
 184 spatial variability of individual orbits and the data record to reduce noise and smooth
 185 spatial gradients in the gridded product. We employed the oversampling approach to
 186 aggregate Level 2 satellite data into a gridded Level 3 product at a 0.1° resolution on
 187 a daily scale. Data from IASI and CrIS were treated separately, but when multiple IASI
 188 and CrIS instruments were available on the same day, their data were merged together.
 189 Each Level 2 pixel was inflated spatially by a factor of 2 along both the major and minor
 190 axes of the ellipses, effectively filling observational gaps and reducing noise. This is a
 191 critical step to enable spatial gradient calculation when data coverage is sparse (e.g.,
 192 only a single overpass is available). This also limits the spatial resolving power to about
 193 twice the pixel size.

194 X and k represent the inverse scale height and chemical reactivity, in which
 195 scale height represents the characteristic height of the species' vertical distribution,
 196 and chemical reactivity represents the inverse of average time before the species
 197 being removed by chemical reactions. To improve the performance of the flux
 198 estimates, we treat the X and k as fundamentally empirical fitting parameters within a
 199 data-driven approach to ensure the resultant emission estimator centers around zero
 200 where emissions are negligible. Although in theory X and k are tied to physically
 201 meaningful quantities, their main purpose is to enhance emission estimators in the
 202 presence of topography and chemistry using information contained by satellite
 203 observations. As such, the quality of fitted X and k is subject to the quality and quantity
 204 of available satellite data. Because of the gaps in individual IASI and CrIS pixels that
 205 lead to undersampling of topography, we expect that X cannot fully account for

206 topography effects over complex terrains, an inherent limitation for scanning Fourier
 207 Transform Spectrometers like IASI and CrIS.

208 In regions where emissions are negligible ($E < 1 \times 10^{-9} \text{ mol m}^{-2} \text{ s}^{-1}$, based on
 209 bottom-up inventory from HEMCO; see Fig. S1 for spatial distribution), Eq. 1 can be
 210 reformulated into a multilinear regression form:

$$211 \quad \langle \vec{u} \cdot (\nabla \Omega) \rangle = \beta_0 + \beta_1 \langle \Omega \vec{u}_0 \cdot (\nabla z_0) \rangle + \beta_2 \langle \Omega \rangle + \varepsilon \quad (2)$$

212 Here β_1 is an estimate of $-X$ and β_2 is an estimate of $-k$. β_0 and ε account for
 213 the offset and random error, in the DD estimator $\langle \vec{u} \cdot (\nabla \Omega) \rangle$. We conducted a two-step
 214 fitting process to estimate X and k following Lonsdale and Sun (2023). The two fitting
 215 processes exclude open water bodies and very rough terrains. The first fitting step
 216 focused on β_1 since the fitting results for β_2 are usually noisy. The first-round fitting for
 217 β_1 was limited in moderately rough terrains with $0.001 \text{ m s}^{-1} < \langle \vec{u}_0 \cdot (\nabla z_0) \rangle < 0.1 \text{ m s}^{-1}$.
 218 Once β_1 was determined and then fixed, the second-round fitting for β_2 was conducted
 219 in flat terrains ($\langle \vec{u}_0 \cdot (\nabla z_0) \rangle < 0.001 \text{ m s}^{-1}$) with moderate NH_3 VCDs ($\Omega > 2.5 \times 10^{-5}$
 220 mol m^{-2}) and minimal emissions ($E < 1 \times 10^{-9} \text{ mol m}^{-2} \text{ s}^{-1}$) to isolate chemical
 221 transformation. To address the challenges associated with a low signal-to-noise ratio,
 222 the fitting was performed over extended time intervals. Daily flux components,
 223 including $\langle \vec{u} \cdot (\nabla \Omega) \rangle$, $\langle \Omega \vec{u}_0 \cdot (\nabla z_0) \rangle$ and $\langle \Omega \rangle$, were first calculated at a spatial resolution
 224 of 0.1° . These values were then aggregated into six-month intervals to improve signal-
 225 to-noise.

226 We tested different spatial groupings, temporal averaging windows, and stricter
 227 maximum emission thresholds to refine the fitted X and k . For X , fitting the entire
 228 domain as a single group produces consistently positive and stable values, whereas
 229 subdividing the domain often introduces excessive noise (Fig. S2). Similarly, varying
 230 the temporal aggregation affects the stability of the fits (Fig. S3): shorter intervals
 231 produce noisier estimates, while longer intervals yield more robust results. We adopted
 232 a six-month aggregation interval as it provides reliable estimates across the entire
 233 period while retaining seasonal variability. The same settings were applied to k for
 234 consistency, though its performance is largely unaffected by these changes (Figs. S4-
 235 S5). Stricter emission thresholds for the chemistry term also have little impact (Fig. S6).

236 2.2.2 Uncertainty in DD estimator

237 To estimate the uncertainty in DD estimator, we calculated DD in both the
 238 zonal/meridional directions (\vec{x}/\vec{y}) and the diagonal directions (\vec{r}/\vec{s}). The final DD value
 239 was determined as the mean of the directional derivatives calculated along the \vec{x}/\vec{y}
 240 and \vec{r}/\vec{s} directions:

$$241 \quad DD = \text{mean}(DD_{\vec{x}/\vec{y}}, DD_{\vec{r}/\vec{s}}) \quad (3)$$

$$242 \quad DD_{\vec{x}/\vec{y}} = \vec{u} \cdot (\nabla \Omega)_{\vec{x}/\vec{y}} = u_x \frac{\partial \Omega}{\partial x} + u_y \frac{\partial \Omega}{\partial y} \quad (4)$$

$$243 \quad DD_{\vec{r}/\vec{s}} = \vec{u} \cdot (\nabla \Omega)_{\vec{r}/\vec{s}} = u_r \frac{\partial \Omega}{\partial r} + u_s \frac{\partial \Omega}{\partial s} \quad (5)$$

244 The difference between $DD_{\bar{x}/\bar{y}}$ and $DD_{\bar{r}/\bar{s}}$ was used to estimate the random
245 errors (σ) of DD :

$$246 \quad \sigma = [\text{std}(DD_{\bar{x}/\bar{y}} - DD_{\bar{r}/\bar{s}})]/2 \quad (6)$$

247 We evaluated NH_3 fluxes at multiple spatial resolutions, including 0.2° , 0.1° , and
248 0.04° . Consistent spatiotemporal patterns are observed across all grid scales (Fig. S7).
249 A resolution of 0.1° is selected as the optimal balance, ensuring sufficient data
250 coverage while effectively capturing spatial gradients in NH_3 fluxes (Wang et al., 2023).

251 **2.3 Spatiotemporal pattern analysis**

252 To analyze the spatial patterns of NH_3 fluxes, we focused on the period from
253 September 2019 to April 2021. This timeframe was selected because both IASI and
254 CrIS observations of NH_3 VCDs provide the most extensive data coverage, enabling a
255 more reliable comparison between the two datasets. We also compared the spatial
256 patterns of satellite-based NH_3 fluxes with bottom-up inventory NH_3 emissions and
257 land cover types. This comparison allows us to evaluate the consistency of satellite-
258 derived flux estimates with known NH_3 sources and their relationship to land use and
259 vegetation cover.

260 For the temporal pattern analysis, we utilized the full observational periods of
261 the datasets: January 2008 to December 2022 for IASI and June 2012 to December
262 2022 for CrIS. This extended temporal coverage allows for a comprehensive
263 understanding of NH_3 flux trends over time. To analyze the temporal patterns of NH_3
264 emission/deposition rates across high-flux regions, we calculated regional
265 emission/deposition rates by spatially integrating the fluxes within the source/sink
266 areas of each region. We examined the seasonal patterns of NH_3 emission/deposition
267 rates in both source and sink areas. These areas were defined based on the
268 uncertainty in DD estimator quantified in Eq. 6. We classified locations where both
269 IASI- and CrIS-derived NH_3 fluxes exceeded 2σ as source regions and locations with
270 both fluxes lower than -2σ as sink regions. Additionally, we investigated the seasonal
271 variations in NH_3 emission/deposition rates derived from IASI and CrIS observations.
272 These were compared with seasonal signals in inventory data to evaluate the
273 consistency between top-down and bottom-up approaches.

274 **3. Results**

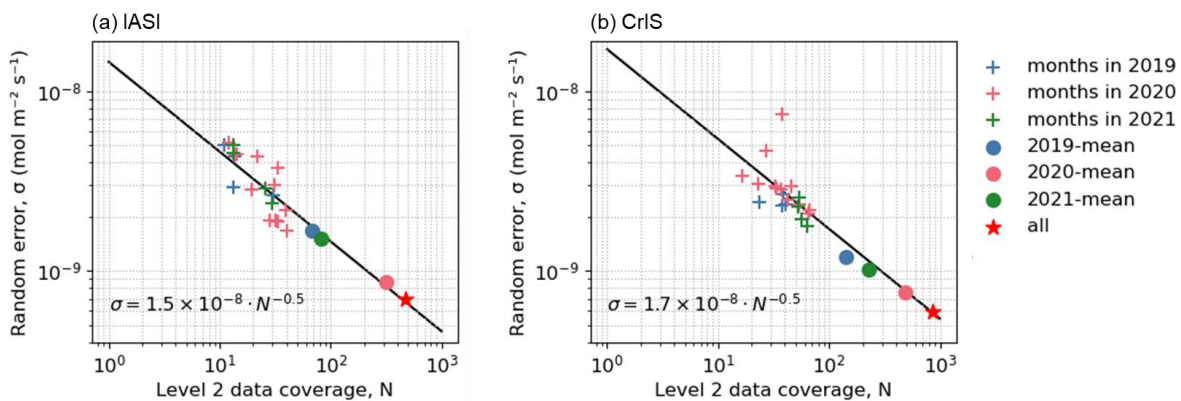
275 **3.1 NH_3 flux estimation**

276 In this study, we used the DD_{chem} estimator as our NH_3 flux estimate. The
277 topography term proves essential for addressing topographic biases in mountainous
278 regions (Fig. S8a, S8b). Estimated NH_3 scale heights generally range from 1 to 2 km
279 (Fig. S9), approximating the planetary boundary layer height. Higher scale heights are
280 observed when only one IASI instrument is operational as well as during winter months
281 in CrIS data, possibly due to weak thermal contrast. The chemistry term contributes
282 strongly in regions with high NH_3 column densities (Fig. S8c, S8d), although the fitted
283 chemical reactivities are generally weak (Fig. S9).

284 Fig. 1 shows the random errors, estimated through Eq. 6, in IASI- (a) and CrIS-
 285 based (b) fluxes. These random errors were calculated separately over monthly,
 286 annual, and total aggregated flux fields and plotted against the mean coverage of Level
 287 2 pixels used in the aggregation. These mean coverage values were denoted by N
 288 and roughly correspond to the number of satellite overpasses. Both IASI and CrIS
 289 observations demonstrate improved precision (lower random errors) with increasing
 290 data coverage. The black lines in Fig. 1 represent the theoretical scaling relationship,
 291 $\sigma = \sigma_0 / \sqrt{N}$, where σ_0 is the scaling factor derived from the random errors of the
 292 monthly values:

$$293 \quad \sigma_0 = \exp(\text{mean}(\log(\sigma_i)) + 0.5 \cdot \text{mean}(\log(N_i))) \quad (7)$$

294 where σ_i and N_i represent the random errors and mean Level 2 data coverage for
 295 month i . If the random errors across different aggregation levels align with the $1/\sqrt{N}$
 296 scaling, it suggests that the random errors are independent and random. This
 297 alignment in Fig. 1 highlights the importance of extensive spatial and temporal
 298 coverage for reliable flux estimation. Additionally, the intercept of the black line with
 299 the vertical line at $N = 1$ provides the theoretical precision (σ_0) of flux estimated by a
 300 single, gap-free overpass of the satellite instrument. IASI shows slightly better single-
 301 overpass precision at $1.5 \times 10^{-8} \text{ mol m}^{-2} \text{ s}^{-1}$ for IASI, compared with $1.7 \times 10^{-8} \text{ mol m}^{-2} \text{ s}^{-1}$
 302 for CrIS. However, the random errors are generally lower for CrIS when aggregated
 303 to the same intervals due to its denser Level 2 coverage than IASI.

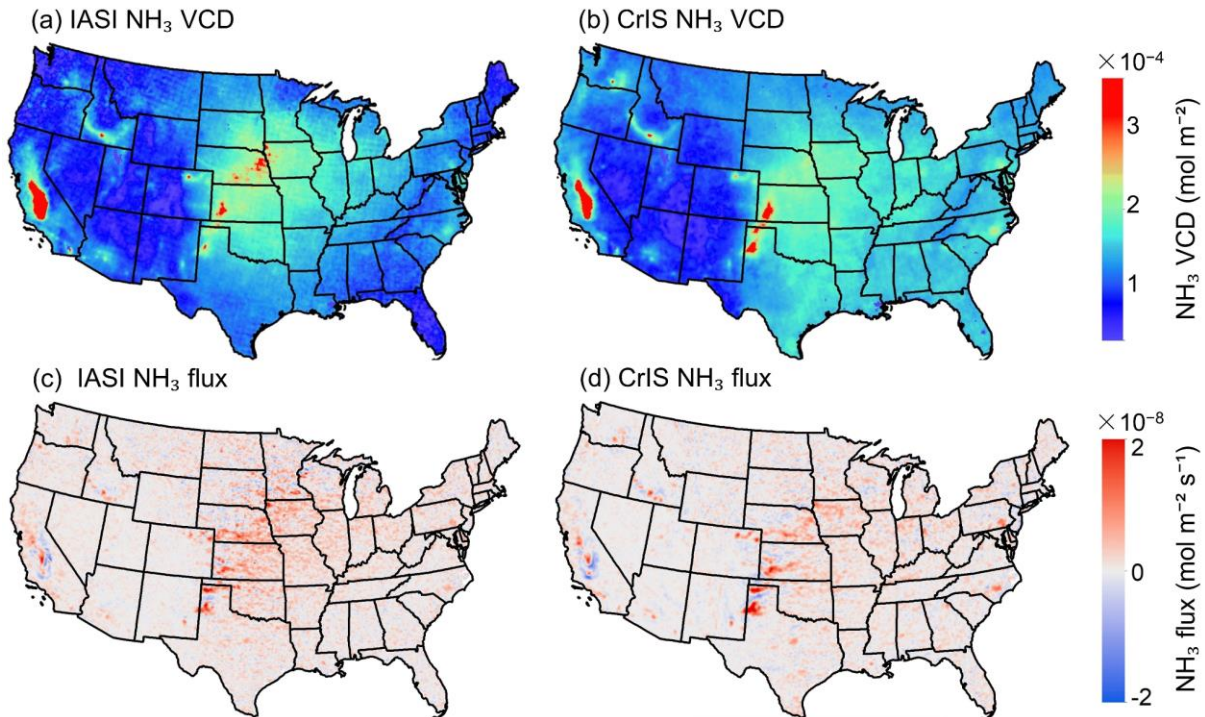


304
 305 Figure 1. The relationship of random error (σ) and data coverage (N) for IASI (a) and
 306 CrIS (b) records from Sep 2019 to Apr 2021. Dots represent random errors at various
 307 aggregation levels (monthly, annual, and total). The black lines represent the
 308 theoretical scaling relationship, $\sigma = \sigma_0 / \sqrt{N}$, where σ_0 denotes the single-overpass
 309 precision.

310 3.2 Spatiotemporal pattern of NH₃ flux over the CONUS

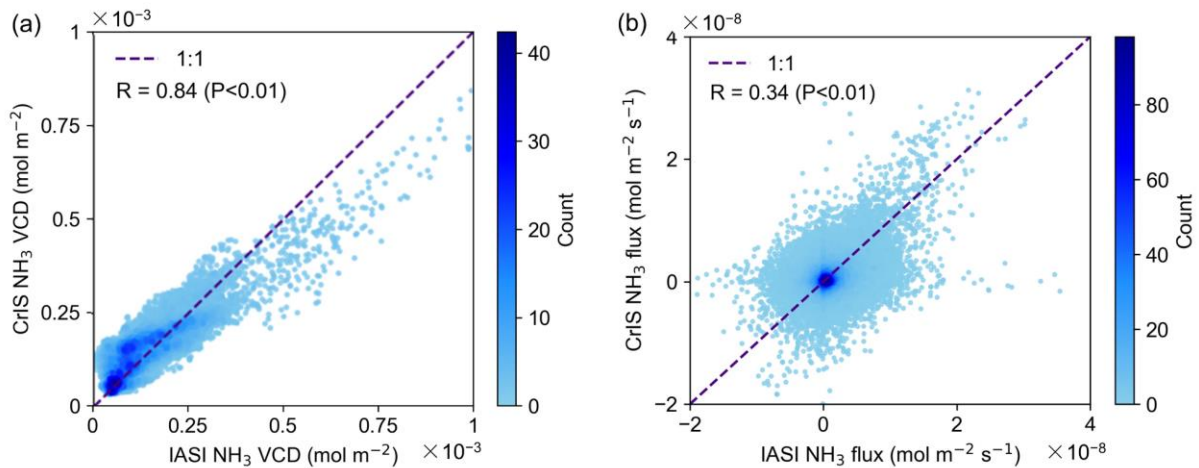
311 IASI and CrIS observations exhibit consistent hotspot regions in NH₃ VCDs and
 312 flux (Fig. 2). Spatially continuous hotspots include the San Joaquin Valley in California,
 313 the Snake River Valley in Idaho, the Texas panhandle and the Great Plains (Figs. 4-
 314 7), all regions known for intensive livestock production and high nitrogen fertilizer use
 315 (Liu et al., 2019). Discrete NH₃ emission hotspots also occur in the eastern United

316 States, notably in Southeastern Pennsylvania and Eastern North Carolina (Figs. 8 and
317 9), where concentrated animal feeding operations (CAFOs) are prevalent. Major NH_3
318 sinks are located near sources, highlighting the localized deposition of NH_3 emissions.
319 The primary sources of NH_3 emissions from satellite observations show strong
320 consistency with those from bottom-up inventories (Fig. S1), enhancing confidence in
321 the reliability of satellite-based flux estimates for identifying key emission regions.



322
323 Figure 2. IASI- (a, c) and CrIS- (b, d) derived NH_3 VCD (a, b) and flux (c, d) averaged
324 from Sep 2019 to Apr 2021 over the CONUS on a 0.1° grid.

325 Both NH_3 VCDs and flux estimates show significant spatial agreement in IASI
326 and CrIS, with correlation coefficients of $R = 0.84$ for VCDs and $R = 0.34$ for NH_3 fluxes
327 ($P < 0.01$; Fig. 3). The VCD comparison reveals systematic differences between IASI
328 and CrIS as different slopes and offsets in different regions (Fig. 3a). These offsets
329 and proportional biases can propagate into flux calculations, where they manifest as
330 amplified variability and reduced correlation (Fig. 3b). The lower correlation in flux
331 estimates compared to VCDs likely reflects compounded noises from derivative-based
332 flux estimates, which relies on external datasets, assumptions, and signal
333 differentiation.



334

335 Figure 3. Comparison of IASI- and CrIS-derived NH₃ VCD (a) and flux (b) averaged
 336 from Sep 2019 to Apr 2021.

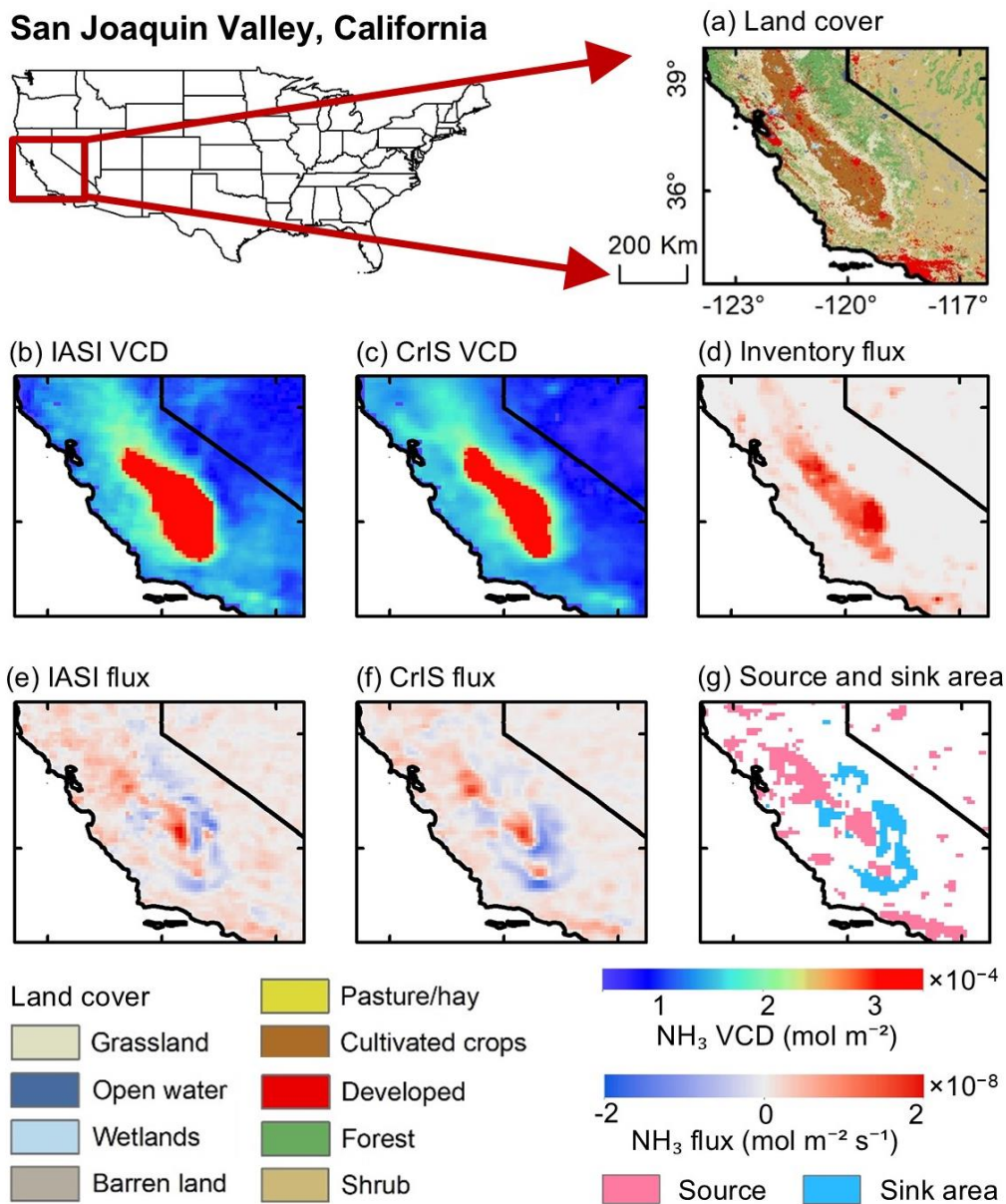
337 **3.3 Spatiotemporal pattern of NH₃ flux in high-flux regions**

338 Figs. 4-9 compare IASI- and CrIS-derived NH₃ fluxes with VCDs and bottom-up
 339 inventories across six major high-flux regions. Application of the flux estimator
 340 substantially sharpens spatial structures relative to VCDs. For instance, in the Snake
 341 River Valley (Fig. 5), enhanced VCDs appear as a broad belt, while the corresponding
 342 fluxes resolve into alternating hot and cold spots, indicating localized source–sink
 343 variability. Similar sharpening is evident in other regions, demonstrating the added
 344 value of the estimator in attributing fluxes to specific land cover types.

345 The two instruments yield broadly consistent spatial patterns of NH₃ source and
 346 sink, although systematic differences are observed. IASI-derived fluxes tend to resolve
 347 finer spatial detail, consistent with its smaller footprint and denser sampling, whereas
 348 CrIS-derived fluxes appear smoother but less noisy. These characteristics are
 349 complementary and together provide robust evidence for the spatial distribution of NH₃
 350 fluxes.

351 Agricultural lands dominate as NH₃ source regions in all cases, with strong
 352 fluxes coinciding with intensive cropping and livestock production (e.g., San Joaquin
 353 Valley, Texas Panhandle, Great Plains). In contrast, natural and semi-natural
 354 landscapes function primarily as sinks. Vegetated landscapes—including forests,
 355 shrublands, and grasslands (Figs. 4-8), as well as wetlands (Fig. 9)—show consistent
 356 negative fluxes, likely reflecting deposition processes in proximity to nearby sources.

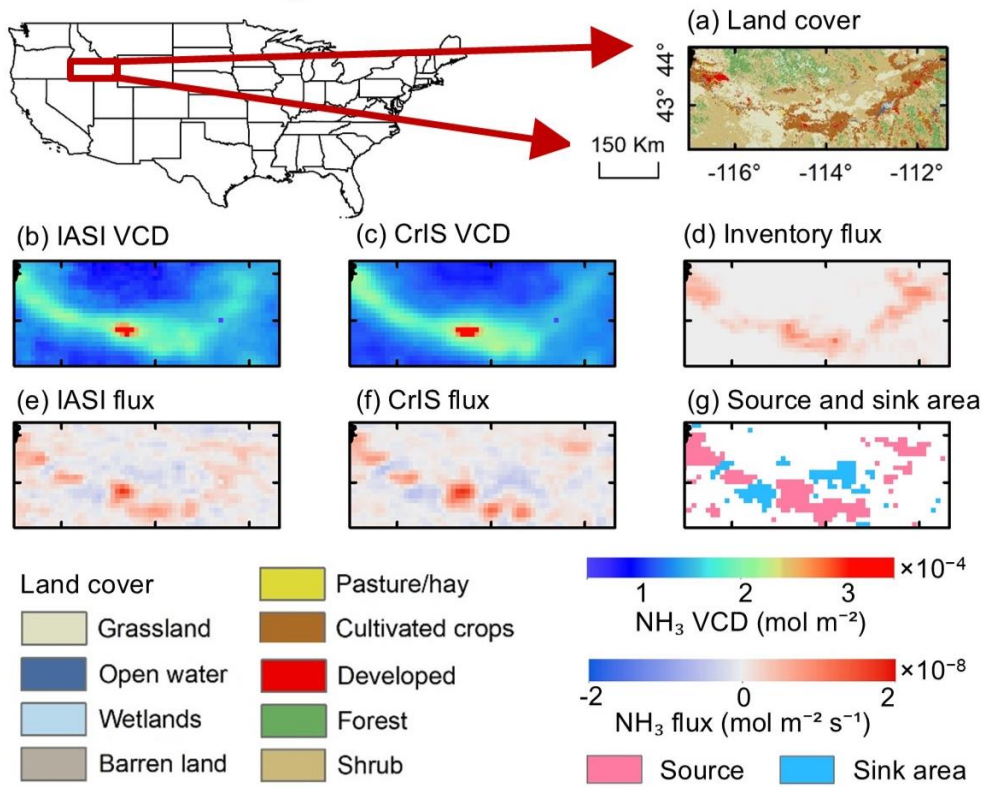
357 Satellite-derived fluxes also align well with bottom-up inventories, with regional
 358 correlation coefficients ranging from 0.08 to 0.86 (Fig. S10). Agreement is highest in
 359 areas with dense agricultural activity (e.g., San Joaquin Valley), whereas
 360 discrepancies in regions such as the Great Plains and Snake River Valley suggest that
 361 inventories may not capture the full subregional variability evident in satellite
 362 observations. These results highlight both the consistency of satellite-derived fluxes
 363 with existing inventories and their capability to provide additional spatial detail.



364

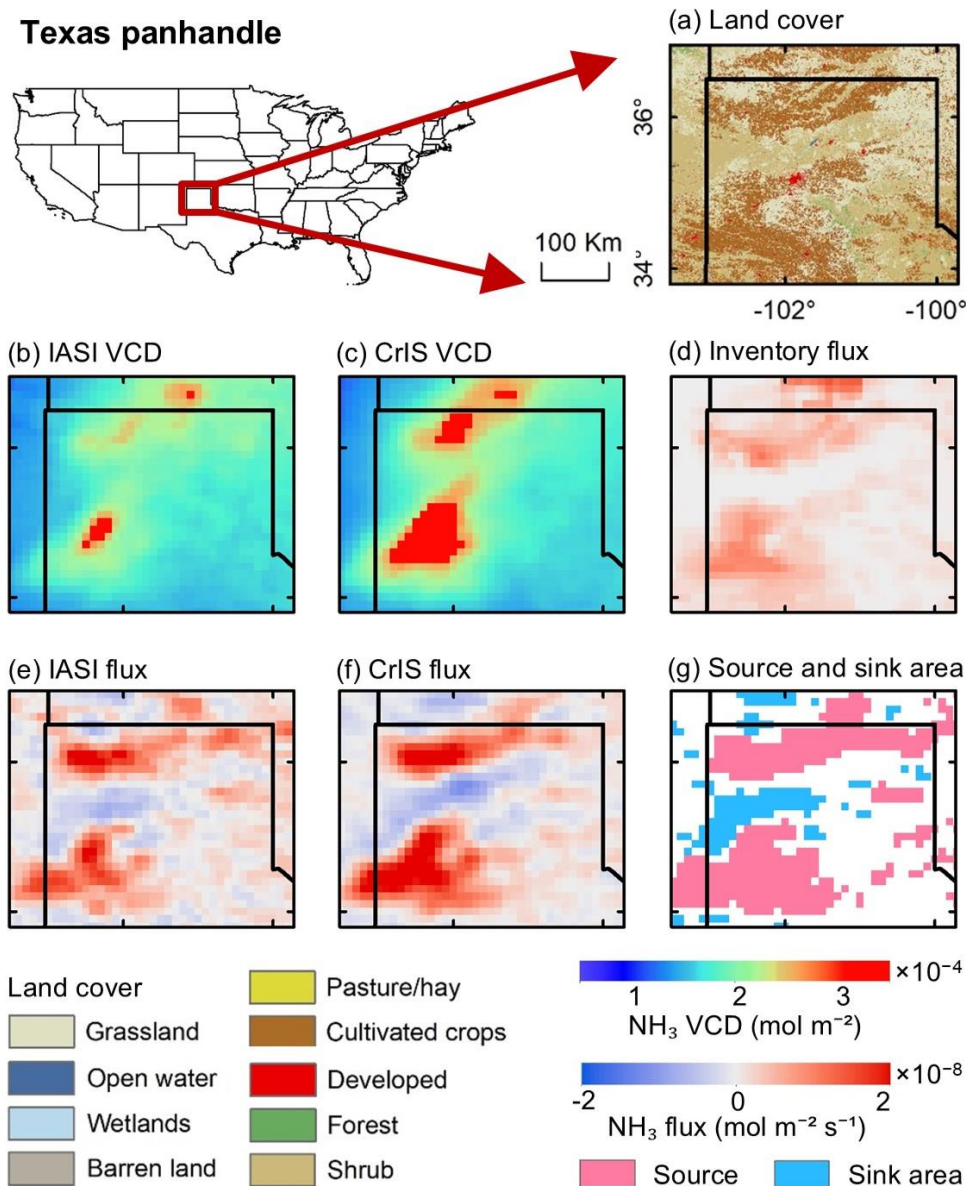
365 Figure 4. (a) Land cover types in the San Joaquin Valley in California. (b, c) VCD and
 366 (e, f) flux derived from IASI and CrIS NH₃ records. (d) NH₃ emission from bottom-up
 367 inventory. (g) Source and sink areas of NH₃ flux, defined as the outside region of $\pm 2\sigma$
 368 of DD from IASI and CrIS.

Snake River Valley, Idaho



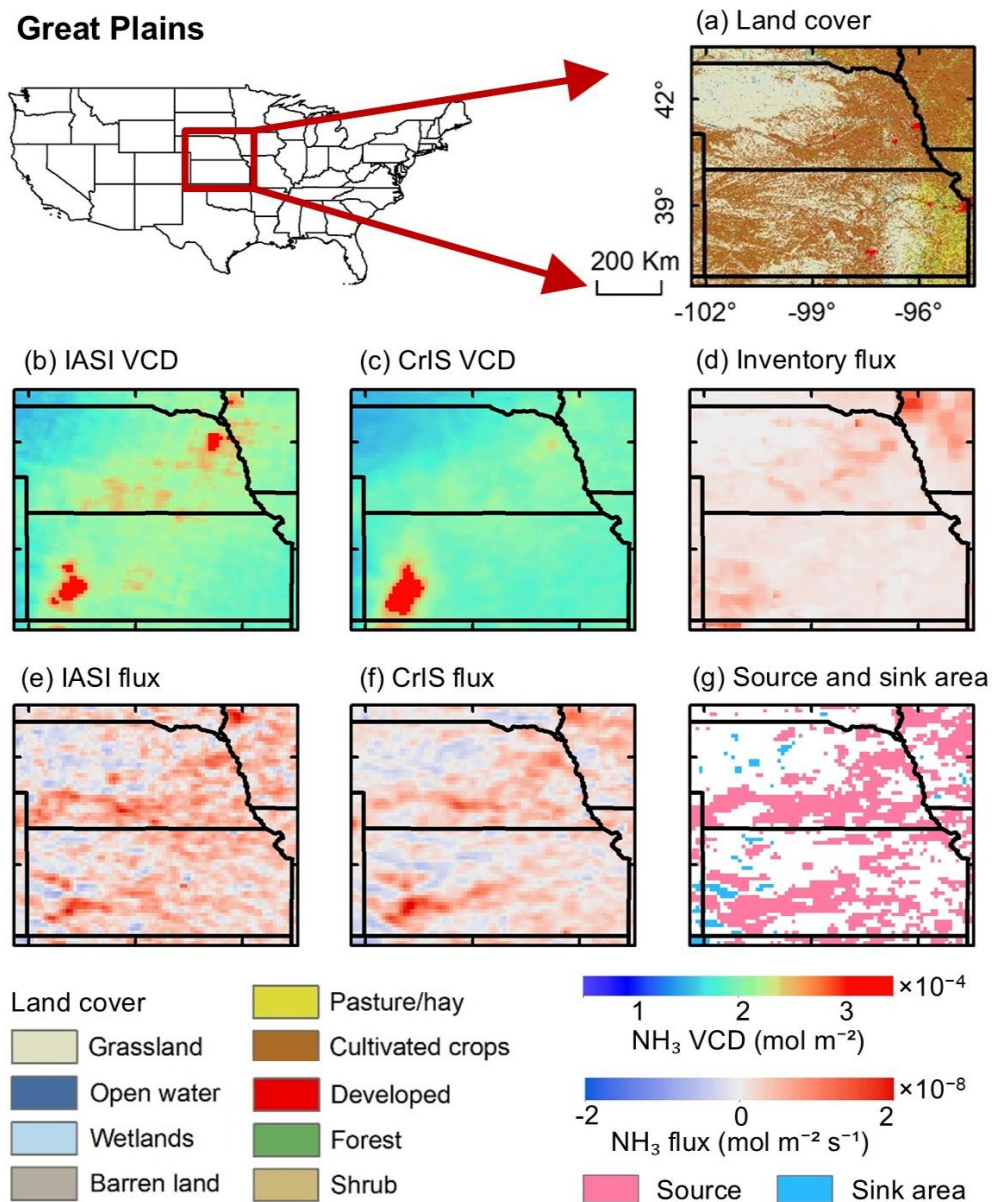
369

370 Figure 5. (a) Land cover types in the Snake River Valley in Idaho. (b, c) VCD and (e,
 371 f) flux derived from IASI and CrIS NH₃ records. (d) NH₃ emission from bottom-up
 372 inventory. (g) Source and sink areas of NH₃ flux, defined as the outside region of $\pm 2\sigma$
 373 of DD from IASI and CrIS.



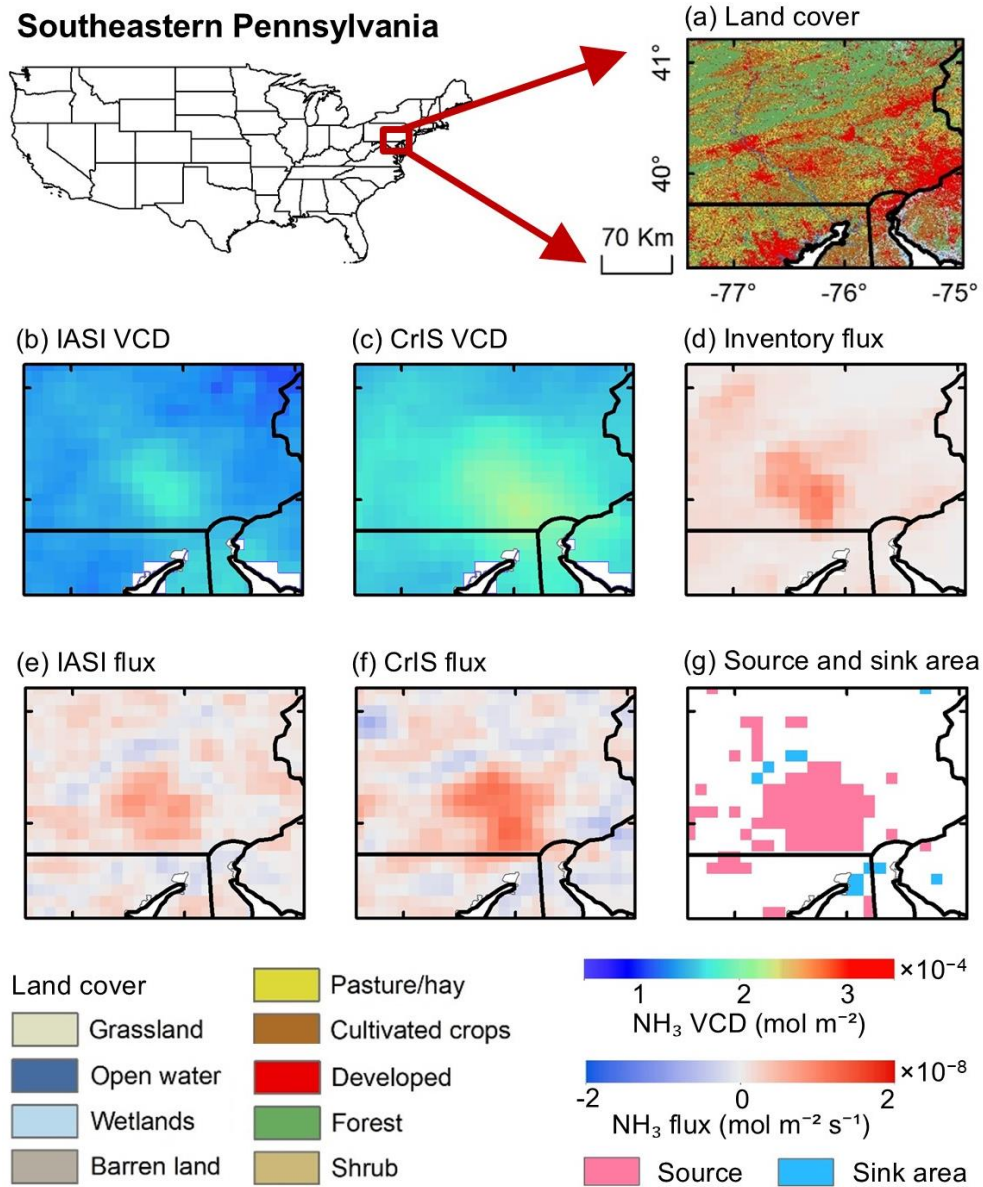
374

375 Figure 6. (a) Land cover types in the Texas panhandle. (b, c) VCD and (e, f) flux
 376 derived from IASI and CrIS NH₃ records. (d) NH₃ emission from bottom-up inventory.
 377 (g) Source and sink areas of NH₃ flux, defined as the outside region of $\pm 2\sigma$ of DD from
 378 IASI and CrIS.



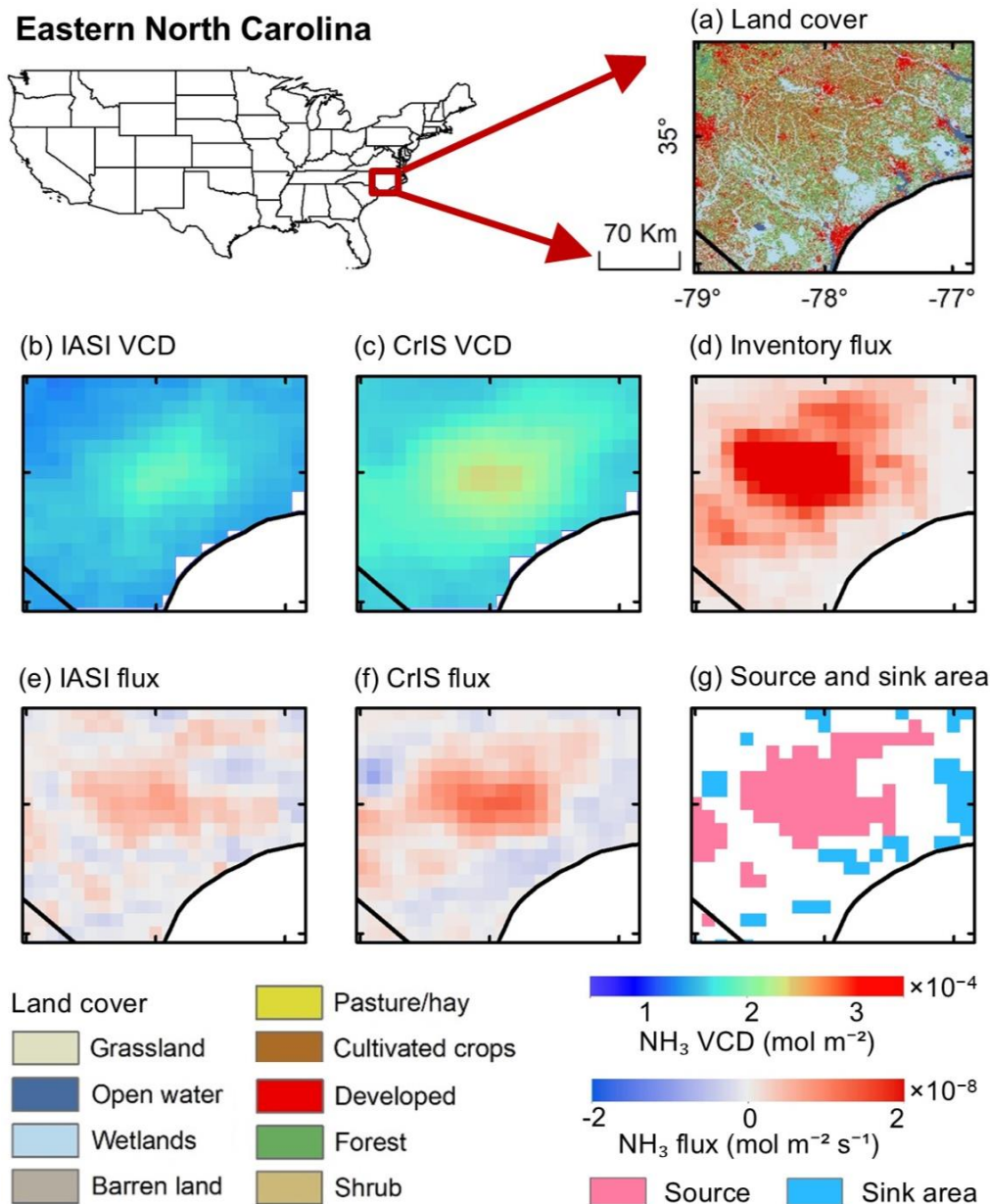
379

380 Figure 7. (a) Land cover types in the Great Plains. (b, c) VCD and (e, f) flux derived
 381 from IASI and CrIS NH₃ records. (d) NH₃ emission from bottom-up inventory. (g)
 382 Source and sink areas of NH₃ flux, defined as the outside region of $\pm 2\sigma$ of DD from
 383 IASI and CrIS.



384

385 Figure 8. (a) Land cover types in Southeastern Pennsylvania. (b, c) VCD and (e, f) flux
 386 derived from IASI and CrIS NH_3 records. (d) NH_3 emission from bottom-up inventory.
 387 (g) Source and sink areas of NH_3 flux, defined as the outside region of $\pm 2\sigma$ of DD from
 388 IASI and CrIS.



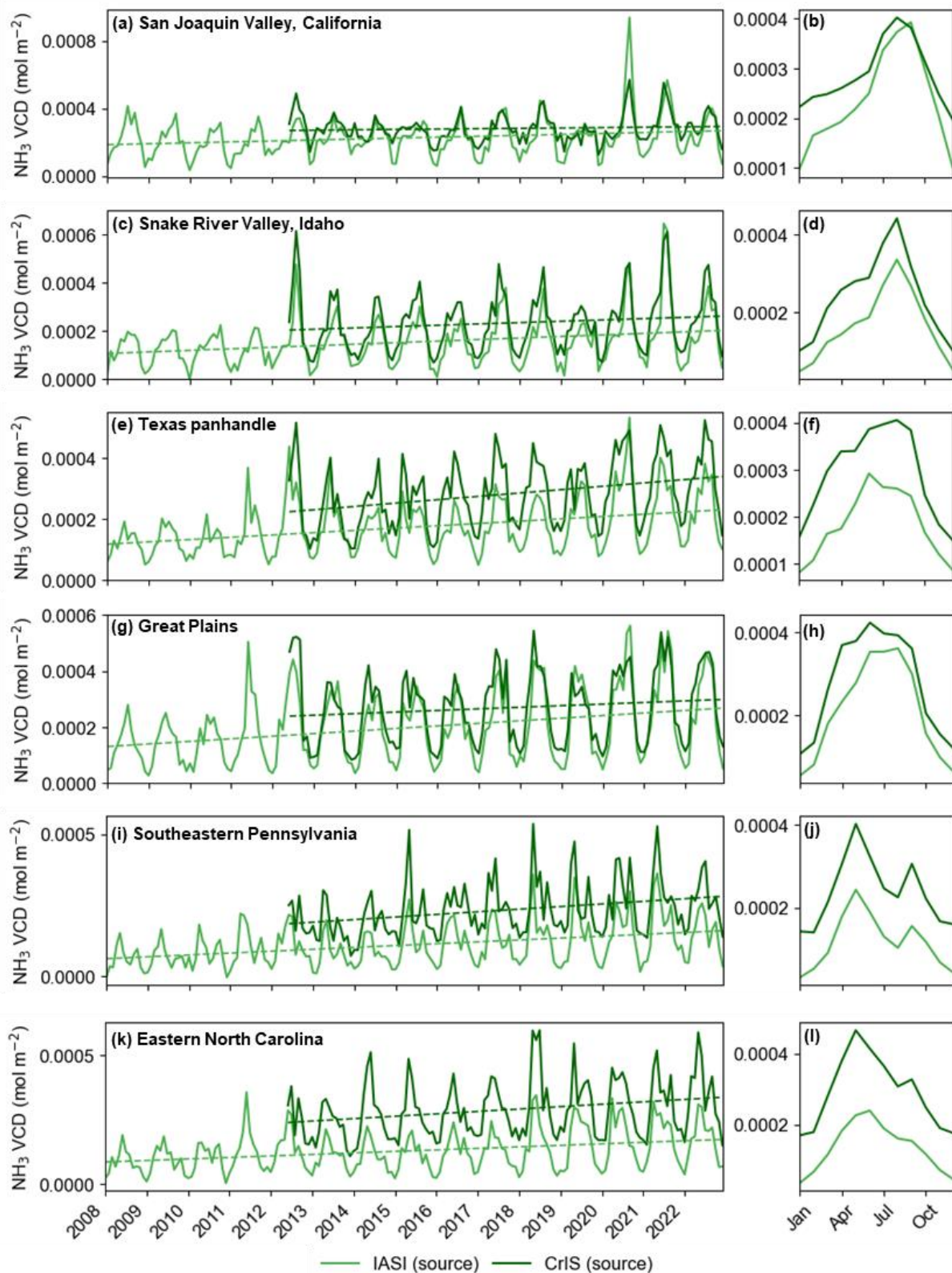
389

390 Figure 9. (a) Land cover types in Eastern North Carolina. (b, c) VCD and (e, f) flux
 391 derived from IASI and CrIS NH₃ records. (d) NH₃ emission from bottom-up inventory.
 392 (g) Source and sink areas of NH₃ flux, defined as the outside region of $\pm 2\sigma$ of DD from
 393 IASI and CrIS.

394 Figs. 10 and 11 illustrate the temporal and seasonal patterns of NH₃ VCDs and
 395 emission/deposition rates across major high-flux regions in the CONUS. Over time,
 396 these regions have exhibited upward trends in VCDs (Fig. 10), potentially indicating
 397 increasing NH₃ emissions. Seasonal cycles in NH₃ VCDs are distinct across all regions,
 398 with higher values in the warm seasons and lower values in winter, driven by increased
 399 agricultural activities, such as livestock operations and fertilizer application, as well as
 400 enhanced volatilization during higher temperatures. Observations from CrIS (dark lines)
 401 and IASI (light lines) are generally aligned, though CrIS often reports higher VCDs.
 402 Differences between CrIS and IASI are largely consistent across seasons, but tend to

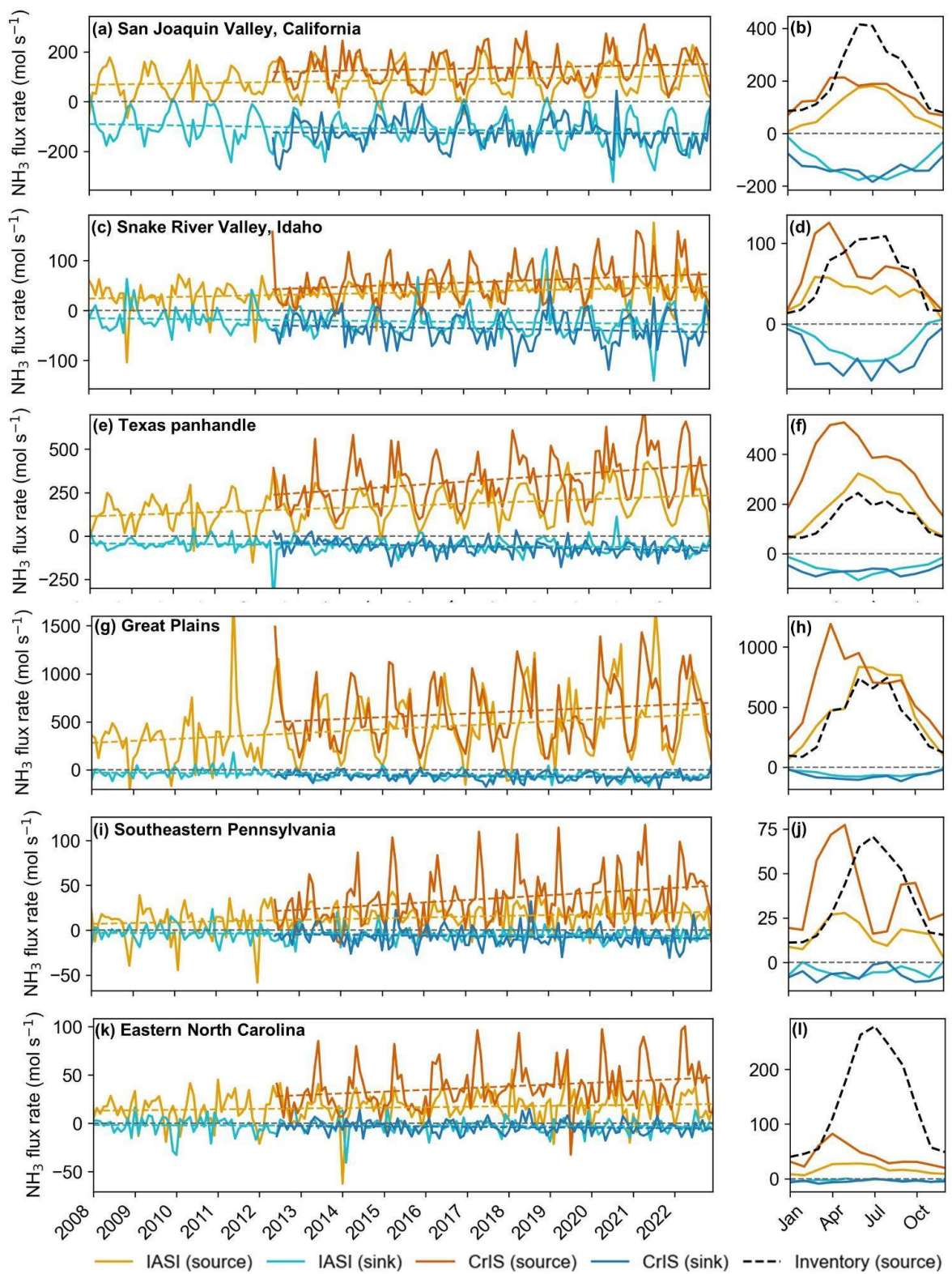
403 be more pronounced in the warm months in regions such as the Texas Panhandle and
404 Great Plains (Fig. 10 f, h).

405 Satellite-derived NH_3 fluxes, including emissions (positive fluxes, yellow lines)
406 and depositions (negative fluxes, blue lines), have exhibited increasing trends over
407 time (Fig. 11). Seasonal patterns in NH_3 fluxes reveal mirrored those of VCDs, with
408 emissions peaking in warm months due to heightened agricultural activity and elevated
409 temperatures, while deposition rates also increase during this period, though with
410 smaller magnitudes. This synchronization between emissions and deposition rates
411 suggests that a significant proportion of emitted NH_3 is deposited locally. A comparison
412 with bottom-up inventory data reveals key differences. Satellite-based estimates
413 capture diurnal patterns, with IASI observing morning emissions (09:30 LST) and CrIS
414 capturing midday emissions (13:30 LST), whereas inventory data represents modeled
415 averages. In regions like the Texas Panhandle and Great Plains (Fig. 11f, h), satellite
416 observations show higher seasonal emission peaks than inventory models, indicating
417 potential underestimation of seasonal emissions in the inventories. Conversely,
418 inventories overestimate emissions compared to satellite observations in the San
419 Joaquin Valley and Eastern North Carolina (Fig. 11b, l). Seasonality in inventory
420 emissions is consistent with IASI observations in some regions, such as the Texas
421 Panhandle and Great Plains (Fig. 11f, h). However, in the Snake River Valley,
422 Southeastern Pennsylvania, and Eastern North Carolina (Fig. 11d, j, l), inventory
423 displays entirely different seasonal signals compared to satellite data, underscoring
424 the value of satellite observations in capturing the temporal dynamics of agricultural
425 emissions. CrIS consistently observes larger NH_3 emissions than IASI, while
426 deposition differences are smaller. Notably, the difference in CrIS and IASI is most
427 obvious in spring across all the regions. CrIS detects early spring peaks in regions
428 such as the Texas Panhandle and Great Plains (Fig. 11f, h), which are not captured
429 by IASI, highlighting variations in sensitivity between the two instruments.



430
 431 Figure 10. Temporal series (a, c, e, g, i, k) and seasonal pattern (b, d, f, h, j, l) of NH₃
 432 VCD at source areas from IASI (light lines) and CrIS (dark lines) records in the San
 433 Joaquin Valley in California (a, b), Snake River Valley in Idaho (c, d), Texas panhandle
 434 (e, f), Great Plains (g, h), Southeastern Pennsylvania (i, j), and Eastern North Carolina

435 (k, l). The dashed lines represent trends derived using linear regression applied to the
 436 monthly temporal series data.



437
 438 Figure 11. Temporal series (a, c, e, g, i, k) and seasonal pattern (b, d, f, h, j, l) of NH₃
 439 emission/deposition rate from IASI (light lines) and CrIS (dark lines) records, and NH₃
 440 emission rate at source areas from bottom-up inventory (black dashed lines) in the

441 San Joaquin Valley in California (a, b), Snake River Valley in Idaho (c, d), Texas
442 panhandle (e, f), Great Plains (g, h), Southeastern Pennsylvania (i, j), and Eastern
443 North Carolina (k, l).

444 **4. Discussion**

445 **4.1 Robustness of satellite-based NH₃ flux estimates**

446 Our findings underscore the value of satellite observations in advancing the
447 characterization of NH₃ fluxes. With the ability to produce flux estimates at relatively
448 fine spatial and temporal scales, satellite datasets can help understand emission and
449 deposition dynamics, thereby providing additional insights into seasonal variability that
450 traditional bottom-up inventories often miss.

451 A key advancement of this work is the combined use of IASI (morning overpass)
452 and CrIS (midday overpass). By combining these two instruments, it is possible to
453 achieve quasi-diurnal coverage and capture the sub-daily variability of NH₃ fluxes that
454 is challenging to discern with a single satellite product. This synergy is especially
455 evident in spring, when the transition from cooler morning to warmer midday conditions
456 can amplify NH₃ emissions. CrIS frequently shows an early-spring emission pulse that
457 is less pronounced in IASI data, especially in areas with substantial emissions (Fig.
458 11). Spring emerges as a critical transitional period, characterized by moderate
459 temperature differences between IASI and CrIS observations (Fig. S11) and relatively
460 high NH₃ fluxes (Fig. 10). This difference may be attributed to the instruments' distinct
461 observational characteristics, such as overpass times, and sensitivities under varying
462 seasonal conditions, and differing detection limits. A further strength of combining
463 different instruments lies in the expanded data coverage. Our error analysis indicates
464 a strong $1/\sqrt{N}$ dependence of random errors (Fig. 1), suggesting that the flux
465 uncertainties drop significantly with denser observations (Wang et al., 2023). By
466 merging multiple overpasses and employing spatial smoothing through physical
467 oversampling, we can substantially reduce random errors and enhance flux reliability.

468 Our satellite-based approach demonstrates some advantages over bottom-up
469 inventories, in which satellite-based observations detect finer-scale fluxes and uncover
470 seasonal patterns not always well represented in inventory data. Previous studies have
471 shown that top-down approaches using satellite observations significantly reduce
472 uncertainties in emission estimates (Byrne et al., 2024; Evangeliou et al., 2021). Each
473 method has unique strengths, and integrating them offers a robust pathway to make
474 more reliable and comprehensive estimates (Tian et al., 2020). While bottom-up
475 methods provide critical context on local processes such as fertilizer application
476 (Zhang et al., 2018), satellite data can validate or refine emission factors and aid in
477 reconciling regional to continental-scale uncertainties (Chen et al., 2021; Zhu et al.,
478 2013).

479 Despite their advantages, infrared-based NH₃ satellite retrievals have certain
480 limitations. Weak thermal contrast and cooler temperatures, especially in winter,
481 reduce detection efficiency (Clarisse et al., 2010; Sutton et al., 2013), and retrievals

482 are limited to daytime clear-sky conditions, potentially biasing results due to NH₃'s
483 strong diurnal cycle (Blanes-Vidal et al., 2008). IASI columns differ from ground-based
484 measurements by $-32 \pm 56\%$ (Dammers et al., 2016), with errors highly dependent on
485 thermal contrast (Van Damme et al., 2014). CrIS retrievals show $\sim 10\text{--}30\%$ error in
486 total columns and larger uncertainty at low concentrations (Shephard et al., 2020).
487 While both IASI and CrIS have demonstrated good long-term stability through
488 calibration monitoring and ground-based validation (Clarisse et al. 2023; Van Damme
489 et al. 2015; Chen et al. 2014; Dammers et al. 2017), subtle time-dependent biases
490 cannot be fully excluded. Overcoming these challenges requires ongoing refinements
491 to retrieval algorithms, particularly in cloud screening and thermal contrast corrections.
492 As satellite missions and retrieval techniques continue to improve, we anticipate further
493 reductions in retrieval biases and increases in data coverage, leading to even more
494 reliable, near real-time estimates of NH₃ fluxes.

495 **4.2 Spatiotemporal pattern of NH₃ flux**

496 Beyond demonstrating robust satellite-based flux estimates, our analysis
497 exposes clear spatial gradients and pronounced seasonality in NH₃ sources and sinks
498 across the CONUS. Both IASI- and CrIS-derived fluxes identify consistent emission
499 hotspots (Fig. 2) in the San Joaquin Valley (California), Snake River Valley (Idaho),
500 Texas Panhandle, Great Plains, Southeastern Pennsylvania, and Eastern North
501 Carolina (Figs. 4-9), characterized by intensive livestock operations and fertilizer
502 application, which are consistent with existing maps of VCD hotspots (Chen et al.,
503 2021; Wang et al., 2021) and emission mapping efforts (Evangeliou et al., 2021; Zhang
504 et al., 2012; Sitwell et al., 2022). Other than emissions, our directional derivariate
505 approach can detect sinks in vegetation-dense areas surrounding these emission
506 sources, such as shrublands and scrublands, forests, grasslands, and wetlands,
507 highlighting the role of nearby ecosystems in capturing NH₃ through deposition (Pan
508 et al., 2021; Hu et al., 2021; Azouz et al., 2019; Kharol et al., 2018; Loubet et al., 2009).
509 Similar hotspots of deposition downwind of intensive agricultural regions have been
510 reported in model-based studies (Ellis et al., 2013; Hu et al., 2021; Zhang et al., 2012).
511 These hotspots often coincide with high NH₃ loadings, large leaf area indices, and
512 micrometeorological conditions favorable for stomatal and cuticular uptake (Sutton et
513 al., 2009). This localized deposition has caused negative effects (e.g., soil acidification,
514 eutrophication, biodiversity loss) in sensitive ecosystems (Krupa, 2003; Pearson and
515 Stewart, 1993). Our results indicate an upward trend in deposition (Fig. 11) that could
516 amplify these impacts in the future.

517 Our results further indicate that deposition near sources is the predominant NH₃
518 removal pathway, rather than chemical transformation. This pattern is likely reflecting
519 acid-limited conditions that suppress the formation of ammonium particulate matter
520 (Pan et al., 2024). The relatively high dry deposition velocity of NH₃ (Hesterberg et al.,
521 1996; Kirchner et al., 2005) and its slow chemical reaction rate with acidic species
522 under acid-limited conditions (Sutton et al., 2009) reinforce the small contribution of
523 chemical pathways to NH₃ removal in many agricultural hotspots. Consistent with

524 recent modeling and observational studies (Luo et al., 2022; Warner et al., 2017), our
525 multi-year analysis reveals a gradual but evident increase in NH₃ fluxes over time (Fig.
526 11), raising concerns that expanding agricultural activities may be offsetting air quality
527 gains achieved through reductions in nitrogen oxides (Li et al., 2016).

528 The seasonality of NH₃ fluxes (Fig. 11) is closely linked to meteorological factors
529 and agricultural activities, with enhanced fluxes in warm months due to increased
530 volatilization from livestock production and fertilizer application (Tang et al., 2018;
531 Warner et al., 2017; Nelson et al., 2017) and relatively lower fluxes in winter. These
532 seasonal signals underscore the importance of timely policy by controlling agricultural
533 practices to manage NH₃ emissions and subsequent environmental impacts.
534 Successful examples from Western Europe demonstrate that targeted regulations can
535 effectively reduce NH₃ emissions (Liu et al., 2022). Furthermore, reducing ammonia
536 emissions proves more cost-effective than controlling nitrogen oxides for mitigating
537 PM_{2.5} pollution (Gu et al., 2021). These findings emphasize the profound influence of
538 agricultural practices and temperature regimes on NH₃ flux dynamics, underscoring
539 the need for integrated strategies to address both local and regional air quality
540 concerns.

541 **5. Conclusion**

542 This study highlights the utility of the directional derivative approach applied to
543 satellite data for estimating NH₃ fluxes across the CONUS. By leveraging IASI and
544 CrIS observations, we address challenges related to spatial variability and seasonal
545 signals, providing insights into NH₃ emission and deposition dynamics.

546 Our findings indicate that deposition serves as a significant removal pathway
547 for NH₃. NH₃ sinks are predominantly located near source regions, particularly in
548 vegetation-dense areas where rapid dry deposition occurs. Major NH₃ emission
549 hotspots are identified in agricultural regions, including the San Joaquin Valley in
550 California, the Snake River Valley in Idaho, the Texas Panhandle, the Great Plains,
551 Southeastern Pennsylvania, and Eastern North Carolina. NH₃ fluxes exhibit a clear
552 seasonal pattern, peaking during warm months due to increased volatilization from
553 agricultural activities and declining during winter with lower temperatures. Increasing
554 trends in NH₃ fluxes highlight the growing impact of intensified agricultural practices,
555 emphasizing the need for improved monitoring and mitigation strategies. While
556 satellite-derived NH₃ fluxes strongly align with bottom-up inventories, satellite
557 observations offer additional value by capturing diurnal variabilities.

558 This study demonstrates the value of satellite observations for high-resolution
559 monitoring of reactive nitrogen cycling, particularly in regions with limited ground-
560 based measurements. These findings offer critical insights for understanding nitrogen
561 loss and deposition processes, supporting enhanced nitrogen management strategies
562 and environmental policy efforts aimed at mitigating ammonia's environmental impacts
563 and managing reactive nitrogen in the atmosphere.

564 **Code and data availability**

565 The IASI L2 ammonia satellite observations are available from the AERIS data
566 infrastructure (<https://doi.org/10.25326/10>, Clarisse et al., 2018). The CrIS L2
567 ammonia satellite observations can be obtained by request to Mark Shephard
568 (mark.shephard@ec.gc.ca). The ERA5 data are available at
569 <https://doi.org/10.24381/cds.adbb2d47> (Hersbach et al., 2023). Code for flux
570 estimation can be found at https://github.com/Kang-Sun-CfA/Oversampling_matlab.
571 The annual ammonia flux dataset derived in this study (2008–2022 for IASI and 2012–
572 2022 for CrIS, 0.1° resolution over the CONUS) is publicly available at Figshare
573 (<https://doi.org/10.6084/m9.figshare.30229648>).

574 **Author contribution**

575 KS and KG designed the study and coordinated the paper. LC, MVD and PFC
576 contributed to the IASI ammonia observations. KCP and MWS provided the CrIS
577 ammonia observations. KS wrote the code for the directional derivative approach. ZL
578 performed the estimations and analyses, and wrote the paper. All the authors
579 contributed to the final version of the paper.

580 **Competing interests**

581 The contact author has declared that neither of the authors has any competing
582 interests.

583 **Acknowledgments**

584 The authors acknowledge support from NASA's Interdisciplinary Science (IDS)
585 Program. KG and ZL acknowledge support from USDA NIFA and Hatch. KS
586 acknowledges support from NSF CAREER (AGS 2338758).

587 **References**

- 588 Adams, C., McLinden, C. A., Shephard, M. W., Dickson, N., Dammers, E., Chen, J., Makar,
589 P., Cady-Pereira, K. E., Tam, N., Kharol, S. K., Lamsal, L. N., and Krotkov, N. A.: Satellite-
590 derived emissions of carbon monoxide, ammonia, and nitrogen dioxide from the 2016
591 Horse River wildfire in the Fort McMurray area, *Atmos. Chem. Phys.*, 19, 2577–2599,
592 <https://doi.org/10.5194/acp-19-2577-2019>, 2019.
- 593 Asman, W. A. H., Sutton, M. A., and Schjørring, J. K.: Ammonia: emission, atmospheric
594 transport and deposition, *New Phytologist*, 139, 27–48, <https://doi.org/10.1046/j.1469-8137.1998.00180.x>, 1998.
- 596 Ayazpour, Z., Sun, K., Zhang, R., and Shen, H.: Evaluation of the directional derivative
597 approach for timely and accurate satellite-based emission estimation using chemical
598 transport model simulation of nitrogen oxides, *J. Geophys. Res.*, 130, e2024JD042817,
599 <https://doi.org/10.1029/2024jd042817>, 2025..
- 600 Azouz, N., Drouet, J.-L., Beekmann, M., Siour, G., Wichink Kruit, R., and Cellier, P.:
601 Comparison of spatial patterns of ammonia concentration and dry deposition flux between
602 a regional Eulerian chemistry-transport model and a local Gaussian plume model, *Air Qual.*
603 *Atmos. Health*, 12, 719–729, <https://doi.org/10.1007/s11869-019-00691-y>, 2019.
- 604 Behera, S. N. and Sharma, M.: Investigating the potential role of ammonia in ion chemistry of
605 fine particulate matter formation for an urban environment, *Sci. Total Environ.*, 408, 3569–
606 3575, <https://doi.org/10.1016/j.scitotenv.2010.04.017>, 2010.
- 607 Beirle, S., Borger, C., Dörner, S., Li, A., Hu, Z., Liu, F., Wang, Y., and Wagner, T.: Pinpointing
608 nitrogen oxide emissions from space, *Sci Adv*, 5, eaax9800,
609 <https://doi.org/10.1126/sciadv.aax9800>, 2019.
- 610 Beirle, S., Borger, C., Dörner, S., Eskes, H., Kumar, V., de Laat, A., and Wagner, T.: Catalog
611 of NO_x emissions from point sources as derived from the divergence of the NO₂ flux for
612 TROPOMI, *Earth Syst. Sci. Data*, 13, 2995–3012, <https://doi.org/10.5194/essd-13-2995-2021>, 2021.
- 614 Blanes-Vidal, V., Hansen, M. N., Pedersen, S., and Rom, H. B.: Emissions of ammonia,
615 methane and nitrous oxide from pig houses and slurry: Effects of rooting material, animal
616 activity and ventilation flow, *Agric. Ecosyst. Environ.*, 124, 237–244,
617 <https://doi.org/10.1016/j.agee.2007.10.002>, 2008.
- 618 Bouwman, A. F., Lee, D. S., Asman, W. A. H., Dentener, F. J., Van Der Hoek, K. W., and
619 Olivier, J. G. J.: A global high-resolution emission inventory for ammonia, *Global*
620 *Biogeochem. Cycles*, 11, 561–587, <https://doi.org/10.1029/97gb02266>, 1997.
- 621 van Breemen, N., Burrough, P. A., Velthorst, E. J., van Dobben, H. F., de Wit, T., Ridder, T.
622 B., and Reijnders, H. F. R.: Soil acidification from atmospheric ammonium sulphate in
623 forest canopy throughfall, *Nature*, 299, 548–550, <https://doi.org/10.1038/299548a0>, 1982.
- 624 Byrne, B., Liu, J., Bowman, K. W., Pascolini-Campbell, M., Chatterjee, A., Pandey, S.,
625 Miyazaki, K., van der Werf, G. R., Wunch, D., Wennberg, P. O., Roehl, C. M., and Sinha,
626 S.: Carbon emissions from the 2023 Canadian wildfires, *Nature*, 633, 835–839,
627 <https://doi.org/10.1038/s41586-024-07878-z>, 2024.
- 628 Cao, H., Henze, D. K., Shephard, M. W., Dammers, E., Cady-Pereira, K., Alvarado, M.,
629 Lonsdale, C., Luo, G., Yu, F., Zhu, L., Danielson, C. G., and Edgerton, E. S.: Inverse

- 630 modeling of NH₃ sources using CrIS remote sensing measurements, *Environ. Res. Lett.*,
631 15, 104082, <https://doi.org/10.1088/1748-9326/abb5cc>, 2020.
- 632 Cao, H., Henze, D. K., Zhu, L., Shephard, M. W., Cady-Pereira, K., Dammers, E., Sitwell, M.,
633 Heath, N., Lonsdale, C., Bash, J. O., Miyazaki, K., Flechard, C., Fauvel, Y., Kruit, R. W.,
634 Feigenspan, S., Brümmer, C., Schrader, F., Twigg, M. M., Leeson, S., Tang, Y. S.,
635 Stephens, A. C. M., Braban, C., Vincent, K., Meier, M., Seitler, E., Geels, C., Ellermann,
636 T., Sanocka, A., and Capps, S. L.: 4D-Var inversion of European NH₃ emissions using
637 CrIS NH₃ measurements and GEOS-chem adjoint with bi-directional and uni-directional
638 flux schemes, *J. Geophys. Res.*, 127, e2021JD035687,
639 <https://doi.org/10.1029/2021JD035687>, 2022.
- 640 Chang, Y., Zou, Z., Deng, C., Huang, K., Collett, J. L., Lin, J., and Zhuang, G.: The importance
641 of vehicle emissions as a source of atmospheric ammonia in the megacity of Shanghai,
642 *Atmos. Chem. Phys.*, 16, 3577–3594, <https://doi.org/10.5194/acp-16-3577-2016>, 2016.
- 643 Chen, Y., Han, Y., Jin, X., and Weng, F.: Assessment of S-NPP CrIS Spectral Calibration
644 Accuracy and Stability, the 94 th AMS Annual Meeting, 2014.
- 645 Chen, Y., Shen, H., Kaiser, J., Hu, Y., Capps, S. L., Zhao, S., Hakami, A., Shih, J.-S., Pavur,
646 G. K., Turner, M. D., Henze, D. K., Resler, J., Nenes, A., Napelenok, S. L., Bash, J. O.,
647 Fahey, K. M., Carmichael, G. R., Chai, T., Clarisse, L., Coheur, P.-F., Van Damme, M.,
648 and Russell, A. G.: High-resolution hybrid inversion of IASI ammonia columns to constrain
649 US ammonia emissions using the CMAQ adjoint model, *Atmos. Chem. Phys.*, 21, 2067–
650 2082, <https://doi.org/10.5194/acp-21-2067-2021>, 2021. Clarisse, L., Shephard, M. W.,
651 Dentener, F., Hurtmans, D., Cady-Pereira, K., Karagulian, F., Van Damme, M., Clerbaux,
652 C., and Coheur, P.-F.: Satellite monitoring of ammonia: A case study of the San Joaquin
653 Valley, *Journal of Geophysical Research: Atmospheres*, 115,
654 <https://doi.org/10.1029/2009JD013291>, 2010.
- 655 Clarisse, L., Van Damme, M., and Coheur, P.-F.: Standard daily IASI/Metop-A ULB-LATMOS
656 ammonia (NH₃) L2 product (total column), <https://doi.org/10.25326/10>, 2018.
- 657 Clarisse, L., Franco, B., Van Damme, M., Di Gioacchino, T., Hadji-Lazaro, J., Whitburn, S.,
658 Noppen, L., Hurtmans, D., Clerbaux, C., and Coheur, P.: The IASI NH₃ version 4 product:
659 averaging kernels and improved consistency, *Atmos. Meas. Tech.*, 16, 5009–5028,
660 <https://doi.org/10.5194/amt-16-5009-2023>, 2023.
- 661 Clerbaux, C., Boynard, A., Clarisse, L., George, M., Hadji-Lazaro, J., Herbin, H., Hurtmans,
662 D., Pommier, M., Razavi, A., Turquety, S., Wespes, C., and Coheur, P.: Monitoring of
663 atmospheric composition using the thermal infrared IASI/METOP sounder, *Atmos. Chem.*
664 *Phys.*, 9, 6041–6054, <https://doi.org/10.5194/ACP-9-6041-2009>, 2009.
- 665 Dammers, E., McLinden, C., Griffin, D., Shephard, M. W., Van Der Graaf, S., Lutsch, E.,
666 Schaap, M., Gainairu-Matz, Y., Fioletov, V. E., Van Damme, M., Whitburn, S., Clarisse,
667 L., Cady-Pereira, K. E., Clerbaux, C., Coheur, P. F., and Willem Erisman, J., NH₃
668 emissions from large point sources derived from CrIS and IASI satellite observations,
669 *Atmos. Chem. Phys.*, 19, 12261–12293, <https://doi.org/10.5194/acp-19-12261-2019>,
670 2019.
- 671 Dammers, E., Palm, M., Van Damme, M., Vigouroux, C., Smale, D., Conway, S., Toon, G. C.,
672 Jones, N., Nussbaumer, E., Warneke, T., Petri, C., Clarisse, L., Clerbaux, C., Hermans,
673 C., Lutsch, E., Strong, K., Hannigan, J. W., Nakajima, H., Morino, I., Herrera, B., Stremme,

- 674 W., Grutter, M., Schaap, M., Wichink Kruit, R. J., Notholt, J., Coheur, P.-F., and Erisman,
675 J. W.: An evaluation of IASI-NH₃ with ground-based Fourier transform infrared
676 spectroscopy measurements, *Atmos. Chem. Phys.*, 16, 10351–10368,
677 <https://doi.org/10.5194/acp-16-10351-2016>, 2016.
- 678 Dammers, E., Shephard, M. W., Palm, M., Cady-Pereira, K., Capps, S., Lutsch, E., Strong, K.,
679 Hannigan, J. W., Ortega, I., Toon, G. C., Stremme, W., Grutter, M., Jones, N., Smale, D.,
680 Siemons, J., Hrpcek, K., Tremblay, D., Schaap, M., Notholt, J., and Erisman, J. W.:
681 Validation of the CrIS fast physical NH₃ retrieval with ground-based FTIR, *Atmos. Meas.*
682 *Tech.*, 10, 2645–2667, <https://doi.org/10.5194/amt-10-2645-2017>, 2017.
- 683 Dentener, F. J. and Crutzen, P. J.: A three-dimensional model of the global ammonia cycle, *J.*
684 *Atmos. Chem.*, 19, 331–369, <https://doi.org/10.1007/bf00694492>, 1994.
- 685 Ellis, R. A., Jacob, D. J., Sulprizio, M. P., Zhang, L., Holmes, C. D., Schichtel, B. A., Blett, T.,
686 Porter, E., Pardo, L. H., and Lynch, J. A.: Present and future nitrogen deposition to
687 national parks in the United States: critical load exceedances, *Atmos. Chem. Phys.*, 13,
688 9083–9095, <https://doi.org/10.5194/acp-13-9083-2013>, 2013.
- 689 Erisman, J. W., Galloway, J. N., Seitzinger, S., Bleeker, A., Dise, N. B., Petrescu, A. M. R.,
690 Leach, A. M., and de Vries, W.: Consequences of human modification of the global
691 nitrogen cycle, *Philos. Trans. R. Soc. Lond. B Biol. Sci.*, 368, 20130116,
692 <https://doi.org/10.1098/rstb.2013.0116>, 2013.
- 693 Evangeliou, N., Balkanski, Y., Eckhardt, S., Cozic, A., Van Damme, M., Coheur, P.-F., Clarisse,
694 L., Shephard, M. W., Cady-Pereira, K. E., and Hauglustaine, D.: 10-year satellite-
695 constrained fluxes of ammonia improve performance of chemistry transport models,
696 *Atmos. Chem. Phys.*, 21, 4431–4451, [https://doi.org/10.5194/acp-21-4431-](https://doi.org/10.5194/acp-21-4431-2021)
697 [202110.5194/acp-21-4431-2021-supplement](https://doi.org/10.5194/acp-21-4431-2021-supplement), 2021.
- 698 Galloway, J. N., Aber, J. D., Erisman, J. W., Seitzinger, S. P., Howarth, R. W., Cowling, E. B.,
699 and Cosby, B. J.: The nitrogen cascade, *Bioscience*, 53, 341,
700 [https://doi.org/10.1641/0006-3568\(2003\)053\[0341:tnc\]2.0.co;2](https://doi.org/10.1641/0006-3568(2003)053[0341:tnc]2.0.co;2), 2003.
- 701 Galloway, J. N., Dentener, F. J., Capone, D. G., Boyer, E. W., Howarth, R. W., Seitzinger, S.
702 P., Asner, G. P., Cleveland, C. C., Green, P. A., Holland, E. A., Karl, D. M., Michaels, A.
703 F., Porter, J. H., Townsend, A. R., and Vöosmarty, C. J.: Nitrogen cycles: Past, present,
704 and future, *Biogeochemistry*, 70, 153–226, <https://doi.org/10.1007/s10533-004-0370-0>,
705 2004.
- 706 Goldberg, D. L., Harkey, M., de Foy, B., Judd, L., Johnson, J., Yarwood, G., and Holloway, T.:
707 Evaluating NO_x emissions and their effect on O₃ production in Texas using TROPOMI
708 NO₂ and HCHO, *Atmos. Chem. Phys.*, 22, 10875–10900, [https://doi.org/10.5194/acp-22-](https://doi.org/10.5194/acp-22-10875-2022)
709 [10875-2022](https://doi.org/10.5194/acp-22-10875-2022), 2022.
- 710 Gong, C., Tian, H., Liao, H., Pan, N., Pan, S., Ito, A., Jain, A. K., Kou-Giesbrecht, S., Joos, F.,
711 Sun, Q., Shi, H., Vuichard, N., Zhu, Q., Peng, C., Maggi, F., Tang, F. H. M., and Zaehle,
712 S.: Global net climate effects of anthropogenic reactive nitrogen, *Nature*, 632, 557–563,
713 <https://doi.org/10.1038/s41586-024-07714-4>, 2024.
- 714 Gu, B., Zhang, L., Van Dingenen, R., Vieno, M., Van Grinsven, H. J., Zhang, X., Zhang, S.,
715 Chen, Y., Wang, S., Ren, C., Rao, S., Holland, M., Winiwarter, W., Chen, D., Xu, J., and
716 Sutton, M. A.: Abating ammonia is more cost-effective than nitrogen oxides for mitigating

- 717 PM2.5 air pollution, *Science*, 374, 758–762, <https://doi.org/10.1126/science.abf8623>,
718 2021.
- 719 Heil, G. W. and Diemont, W. H.: Raised nutrient levels change heathland into grassland,
720 *Vegetatio*, 53, 113–120, <https://doi.org/10.1007/bf00043031>, 1983.
- 721 Hersbach, H., Bell, B., Berrisford, P., Hirahara, S., Horányi, A., Muñoz-Sabater, J., Nicolas, J.,
722 Peubey, C., Radu, R., Schepers, D., Simmons, A., Soci, C., Abdalla, S., Abellan, X.,
723 Balsamo, G., Bechtold, P., Biavati, G., Bidlot, J., Bonavita, M., De Chiara, G., Dahlgren,
724 P., Dee, D., Diamantakis, M., Dragani, R., Flemming, J., Forbes, R., Fuentes, M., Geer,
725 A., Haimberger, L., Healy, S., Hogan, R. J., Hólm, E., Janisková, M., Keeley, S., Laloyaux,
726 P., Lopez, P., Lupu, C., Radnoti, G., de Rosnay, P., Rozum, I., Vamborg, F., Villaume, S.,
727 and Jean-Noël Thépaut: The ERA5 global reanalysis, *Quart. J. Roy. Meteor. Soc.*, 146,
728 1999–2049, <https://doi.org/10.1002/qj.3803>, 2020.
- 729 Hersbach, H., Bell, B., Berrisford, P., Biavati, G., Horányi, A., Muñoz-Sabater, J., Nicolas, J.,
730 Peubey, C., Radu, R., Rozum, I., Schepers, D., Simmons, A., Soci, C., Dee, D., and
731 Thépaut, J.-N.: ERA5 hourly data on single levels from 1940 to present,
732 <https://doi.org/10.24381/CDS.ADBB2D47>, 2023.
- 733 Hesterberg, R., Blatter, A., Fahrni, M., Rosset, M., Nefel, A., Eugster, W., and Wanner, H.:
734 Deposition of nitrogen-containing compounds to an extensively managed grassland in
735 central Switzerland, *Environ. Pollut.*, 91, 21–34, [https://doi.org/10.1016/0269-7491\(95\)00036-q](https://doi.org/10.1016/0269-7491(95)00036-q), 1996.
- 737 Hu, C., Griffis, T. J., Frie, A., Baker, J. M., Wood, J. D., Millet, D. B., Yu, Z., Yu, X., and
738 Czarnetzki, A. C.: A multiyear constraint on ammonia emissions and deposition within the
739 US corn belt, *Geophys. Res. Lett.*, 48, e2020GL090865,
740 <https://doi.org/10.1029/2020gl090865>, 2021.
- 741 Kharol, S. K., Shephard, M. W., McLinden, C. A., Zhang, L., Sioris, C. E., O'Brien, J. M., Vet,
742 R., Cady-Pereira, K. E., Hare, E., Siemons, J., and Krotkov, N. A.: Dry deposition of
743 reactive nitrogen from satellite observations of ammonia and nitrogen dioxide over north
744 America, *Geophys. Res. Lett.*, 45, 1157–1166, <https://doi.org/10.1002/2017gl075832>,
745 2018.
- 746 Kirchner, M., Jakobi, G., Feicht, E., Bernhardt, M., and Fischer, A.: Elevated NH₃ and NO₂ air
747 concentrations and nitrogen deposition rates in the vicinity of a highway in Southern
748 Bavaria, *Atmos. Environ.* (1994), 39, 4531–4542,
749 <https://doi.org/10.1016/j.atmosenv.2005.03.052>, 2005.
- 750 Krupa, S. V.: Effects of atmospheric ammonia (NH₃) on terrestrial vegetation: a review,
751 *Environ. Pollut.*, 124, 179–221, [https://doi.org/10.1016/s0269-7491\(02\)00434-7](https://doi.org/10.1016/s0269-7491(02)00434-7), 2003.
- 752 Lin, H., Jacob, D. J., Lundgren, E. W., Sulprizio, M. P., Keller, C. A., Fritz, T. M., Eastham, S.
753 D., Emmons, L. K., Campbell, P. C., Baker, B., Saylor, R. D., and Montuoro, R.:
754 Harmonized Emissions Component (HEMCO) 3.0 as a versatile emissions component for
755 atmospheric models: application in the GEOS-Chem, NASA GEOS, WRF-GC, CESM2,
756 NOAA GEFS-Aerosol, and NOAA UFS models, *Geosci. Model Dev.*, 14, 5487–5506,
757 <https://doi.org/10.5194/gmd-14-5487-2021>, 2021.
- 758 Liu, L., Zhang, X., Wong, A. Y. H., Xu, W., Liu, X., Li, Y., Mi, H., Lu, X., Zhao, L., Wang, Z.,
759 Wu, X., and Wei, J.: Estimating global surface ammonia concentrations inferred from

- 760 satellite retrievals, *Atmos. Chem. Phys.*, 19, 12051–12066, [https://doi.org/10.5194/acp-](https://doi.org/10.5194/acp-19-12051-2019)
761 19-12051-2019, 2019.
- 762 Liu, L., Xu, W., Lu, X., Zhong, B., Guo, Y., Lu, X., Zhao, Y., He, W., Wang, S., Zhang, X., Liu,
763 X., and Vitousek, P.: Exploring global changes in agricultural ammonia emissions and
764 their contribution to nitrogen deposition since 1980, *Proc. Natl. Acad. Sci. U. S. A.*, 119,
765 e2121998119, <https://doi.org/10.1073/pnas.2121998119>, 2022.
- 766 Li, Y., Schichtel, B. A., Walker, J. T., Schwede, D. B., Chen, X., Lehmann, C. M. B., Puchalski,
767 M. A., Gay, D. A., and Collett, J. L., Jr: Increasing importance of deposition of reduced
768 nitrogen in the United States, *Proc. Natl. Acad. Sci. U. S. A.*, 113, 5874–5879,
769 <https://doi.org/10.1073/pnas.1525736113>, 2016.
- 770 Lonsdale, C. R. and Sun, K.: Nitrogen oxides emissions from selected cities in North America,
771 Europe, and East Asia observed by the TROPOspheric Monitoring Instrument (TROPOMI)
772 before and after the COVID-19 pandemic, *Atmos. Chem. Phys.*, 23, 8727–8748,
773 <https://doi.org/10.5194/acp-23-8727-2023>, 2023.
- 774 Loubet, B., Asman, W. A. H., Theobald, M. R., Hertel, O., Tang, Y. S., Robin, P., Hassouna,
775 M., Dämmgen, U., Genermont, S., Cellier, P., and Sutton, M. A.: Ammonia deposition
776 near hot spots: Processes, models and monitoring methods, in: *Atmospheric Ammonia*,
777 Springer Netherlands, Dordrecht, 205–267, [https://doi.org/10.1007/978-1-4020-9121-](https://doi.org/10.1007/978-1-4020-9121-6_15)
778 6_15, 2009.
- 779 Luo, Z., Zhang, Y., Chen, W., Van Damme, M., Coheur, P.-F., and Clarisse, L.: Estimating
780 global ammonia (NH₃) emissions based on IASI observations from 2008 to 2018, *Atmos.*
781 *Chem. Phys.*, 22, 10375–10388, <https://doi.org/10.5194/acp-22-10375-2022>, 2022.
- 782 Ma, R., Li, K., Guo, Y., Zhang, B., Zhao, X., Linder, S., Guan, C., Chen, G., Gan, Y., and Meng,
783 J.: Mitigation potential of global ammonia emissions and related health impacts in the
784 trade network, *Nat. Commun.*, 12, 6308, <https://doi.org/10.1038/s41467-021-25854-3>,
785 2021.
- 786 Marais, E. A., Pandey, A. K., Van Damme, M., Clarisse, L., Coheur, P.-F., Shephard, M. W.,
787 Cady-Pereira, K. E., Misselbrook, T., Zhu, L., Luo, G., and Yu, F.: UK ammonia emissions
788 estimated with satellite observations and GEOS-chem, *J. Geophys. Res.*, 126,
789 <https://doi.org/10.1029/2021jd035237>, 2021.
- 790 Nelson, A. J., Koloutsou-Vakakis, S., Rood, M. J., Myles, L., Lehmann, C., Bernacchi, C.,
791 Balasubramanian, S., Joo, E., Heuer, M., Vieira-Filho, M., and Lin, J.: Season-long
792 ammonia flux measurements above fertilized corn in central Illinois, USA, using relaxed
793 eddy accumulation, *Agric. For. Meteorol.*, 239, 202–212,
794 <https://doi.org/10.1016/j.agrformet.2017.03.010>, 2017.
- 795 Pan, D., Benedict, K. B., Golston, L. M., Wang, R., Collett, J. L., Jr, Tao, L., Sun, K., Guo, X.,
796 Ham, J., Prenni, A. J., Schichtel, B. A., Mikoviny, T., Müller, M., Wisthaler, A., and Zondlo,
797 M. A.: Ammonia dry deposition in an alpine ecosystem traced to agricultural emission
798 hotspots, *Environ. Sci. Technol.*, 55, 7776–7785, <https://doi.org/10.1021/acs.est.0c05749>,
799 2021.
- 800 Pan, D., Mauzerall, D. L., Wang, R., Guo, X., Puchalski, M., Guo, Y., Song, S., Tong, D.,
801 Sullivan, A. P., Schichtel, B. A., Collett, J. L., Jr, and Zondlo, M. A.: Regime shift in
802 secondary inorganic aerosol formation and nitrogen deposition in the rural United States,

- 803 Nat. Geosci., 17, 617–623, <https://doi.org/10.1038/s41561-024-01455-9>, 2024.
- 804 Pearson, J. and Stewart, G. R.: The deposition of atmospheric ammonia and its effects on
805 plants, *New Phytol.*, 125, 283–305, <https://doi.org/10.1111/j.1469-8137.1993.tb03882.x>,
806 1993.
- 807 Reche, C., Viana, M., Karanasiou, A., Cusack, M., Alastuey, A., Artiñano, B., Revuelta, M. A.,
808 López-Mahía, P., Blanco-Heras, G., Rodríguez, S., Sánchez de la Campa, A. M.,
809 Fernández-Camacho, R., González-Castanedo, Y., Mantilla, E., Tang, Y. S., and Querol,
810 X.: Urban NH₃ levels and sources in six major Spanish cities, *Chemosphere*, 119, 769–
811 777, <https://doi.org/10.1016/j.chemosphere.2014.07.097>, 2015.
- 812 Shephard, M. W. and Cady-Pereira, K.E.: Cross-track Infrared Sounder (CrIS) Satellite
813 Observations of Tropospheric Ammonia, *Atmos. Meas. Tech.*, 8, 1323–1336,
814 <https://doi.org/10.5194/amt-8-1323-2015>, 2015.
- 815 Shephard, M. W., Dammers, E., Cady-Pereira, K. E., Kharol, S. K., Thompson, J., Gainariu-
816 Matz, Y., Zhang, J., McLinden, C. A., Kovachik, A., Moran, M., Bittman, S., Sioris, C. E.,
817 Griffin, D., Alvarado, M. J., Lonsdale, C., Savic-Jovicic, V., and Zheng, Q.: Ammonia
818 measurements from space with the Cross-track Infrared Sounder: characteristics and
819 applications, *Atmos. Chem. Phys.*, 20, 2277–2302, [https://doi.org/10.5194/acp-20-2277-](https://doi.org/10.5194/acp-20-2277-2020)
820 2020, 2020.
- 821 Sitwell, M., Shephard, M. W., Rochon, Y., Cady-Pereira, K., and Dammers, E.: An ensemble-
822 variational inversion system for the estimation of ammonia emissions using CrIS satellite
823 ammonia retrievals, *Atmos. Chem. Phys.*, 22, 6595–6624, [https://doi.org/10.5194/acp-22-](https://doi.org/10.5194/acp-22-6595-2022)
824 6595-2022, 2022.
- 825 Sommer, S. G., Olesen, J. E., and Christensen, B. T.: Effects of temperature, wind speed and
826 air humidity on ammonia volatilization from surface applied cattle slurry, *J. Agric. Sci.*, 117,
827 91–100, <https://doi.org/10.1017/S0021859600079016>, 1991.
- 828 Sun, K.: Derivation of emissions from satellite-observed column amounts and its application
829 to TROPOMI NO₂ and CO observations, *Geophys. Res. Lett.*, 49,
830 <https://doi.org/10.1029/2022gl101102>, 2022.
- 831 Sun, K., Tao, L., Miller, D. J., Pan, D., Golston, L. M., Zondlo, M. A., Griffin, R. J., Wallace, H.
832 W., Leong, Y. J., Yang, M. M., Zhang, Y., Mauzerall, D. L., and Zhu, T.: Vehicle emissions
833 as an important urban ammonia source in the United States and China, *Environ. Sci.*
834 *Technol.*, 51, 2472–2481, <https://doi.org/10.1021/acs.est.6b02805>, 2017.
- 835 Sun, K., Zhu, L., Cady-Pereira, K., Chan Miller, C., Chance, K., Clarisse, L., Coheur, P.-F.,
836 González Abad, G., Huang, G., Liu, X., Van Damme, M., Yang, K., and Zondlo, M.: A
837 physics-based approach to oversample multi-satellite, multispecies observations to a
838 common grid, *Atmos. Meas. Tech.*, 11, 6679–6701, [https://doi.org/10.5194/amt-11-6679-](https://doi.org/10.5194/amt-11-6679-2018)
839 2018, 2018.
- 840 Sutton, M., Reis, S., and Baker, S. (Eds.): *Atmospheric Ammonia: Detecting emission changes
841 and environmental impacts. Results of an Expert Workshop under the Convention on
842 Long-range Transboundary Air Pollution*, 1st ed., Springer, New York, NY, 464 pp.,
843 <https://doi.org/10.1007/978-1-4020-9121-6>, 2009.
- 844 Sutton, M. A., Erisman, J. W., Dentener, F., and Möller, D.: Ammonia in the environment: from
845 ancient times to the present, *Environ. Pollut.*, 156, 583–604,

- 846 <https://doi.org/10.1016/j.envpol.2008.03.013>, 2008.
- 847 Sutton, M. A., Reis, S., Riddick, S. N., Dragosits, U., Nemitz, E., Theobald, M. R., Tang, Y. S.,
848 Braban, C. F., Vieno, M., Dore, A. J., Mitchell, R. F., Wanless, S., Daunt, F., Fowler, D.,
849 Blackall, T. D., Milford, C., Flechard, C. R., Loubet, B., Massad, R., Cellier, P., Personne,
850 E., Coheur, P. F., Clarisse, L., Van Damme, M., Ngadi, Y., Clerbaux, C., Skjøth, C. A.,
851 Geels, C., Hertel, O., Wichink Kruit, R. J., Pinder, R. W., Bash, J. O., Walker, J. T.,
852 Simpson, D., Horváth, L., Misselbrook, T. H., Bleeker, A., Dentener, F., and de Vries, W.:
853 Towards a climate-dependent paradigm of ammonia emission and deposition, *Philos.*
854 *Trans. R. Soc. Lond. B Biol. Sci.*, 368, 20130166, <https://doi.org/10.1098/rstb.2013.0166>,
855 2013.
- 856 Sutton, M. A., van Dijk, N., Levy, P. E., Jones, M. R., Leith, I. D., Sheppard, L. J., Leeson, S.,
857 Sim Tang, Y., Stephens, A., Braban, C. F., Dragosits, U., Howard, C. M., Vieno, M., Fowler,
858 D., Corbett, P., Naikoo, M. I., Munzi, S., Ellis, C. J., Chatterjee, S., Steadman, C. E.,
859 Móríng, A., and Wolseley, P. A.: Alkaline air: changing perspectives on nitrogen and air
860 pollution in an ammonia-rich world, *Philos. Trans. A Math. Phys. Eng. Sci.*, 378, 20190315,
861 <https://doi.org/10.1098/rsta.2019.0315>, 2020.
- 862 Tang, Y. S., Braban, C. F., Dragosits, U., Dore, A. J., Simmons, I., van Dijk, N., Poskitt, J., Dos
863 Santos Pereira, G., Keenan, P. O., Conolly, C., Vincent, K., Smith, R. I., Heal, M. R., and
864 Sutton, M. A.: Drivers for spatial, temporal and long-term trends in atmospheric ammonia
865 and ammonium in the UK, *Atmos. Chem. Phys.*, 18, 705–733, [https://doi.org/10.5194/acp-](https://doi.org/10.5194/acp-18-705-2018)
866 [18-705-2018](https://doi.org/10.5194/acp-18-705-2018), 2018.
- 867 Tian, H., Xu, R., Canadell, J. G., Thompson, R. L., Winiwarter, W., Suntharalingam, P.,
868 Davidson, E. A., Ciais, P., Jackson, R. B., Janssens-Maenhout, G., Prather, M. J., Regnier,
869 P., Pan, N., Pan, S., Peters, G. P., Shi, H., Tubiello, F. N., Zaehle, S., Zhou, F., Arneeth,
870 A., Battaglia, G., Berthet, S., Bopp, L., Bouwman, A. F., Buitenhuis, E. T., Chang, J.,
871 Chipperfield, M. P., Dangal, S. R. S., Dlugokencky, E., Elkins, J. W., Eyre, B. D., Fu, B.,
872 Hall, B., Ito, A., Joos, F., Krummel, P. B., Landolfi, A., Laruelle, G. G., Lauerwald, R., Li,
873 W., Lienert, S., Maavara, T., MacLeod, M., Millet, D. B., Olin, S., Patra, P. K., Prinn, R.
874 G., Raymond, P. A., Ruiz, D. J., van der Werf, G. R., Vuichard, N., Wang, J., Weiss, R.
875 F., Wells, K. C., Wilson, C., Yang, J., and Yao, Y.: A comprehensive quantification of
876 global nitrous oxide sources and sinks, *Nature*, 586, 248–256,
877 <https://doi.org/10.1038/s41586-020-2780-0>, 2020.
- 878 Van Damme, M., Clarisse, L., Heald, C. L., Hurtmans, D., Ngadi, Y., Clerbaux, C., Dolman, A.
879 J., Erisman, J. W., and Coheur, P. F.: Global distributions, time series and error
880 characterization of atmospheric ammonia (NH₃) from IASI satellite observations, *Atmos.*
881 *Chem. Phys.*, 14, 2905–2922, <https://doi.org/10.5194/acp-14-2905-2014>, 2014.
- 882 Van Damme, M., Clarisse, L., Dammers, E., Liu, X., Nowak, J. B., Clerbaux, C., Flechard, C.
883 R., Galy-Lacaux, C., Xu, W., Neuman, J. A., Tang, Y. S., Sutton, M. A., Erisman, J. W.,
884 and Coheur, P. F.: Towards validation of ammonia (NH₃) measurements from the IASI
885 satellite, *Atmos. Meas. Tech.*, 8, 1575–1591, <https://doi.org/10.5194/amt-8-1575-2015>,
886 2015.
- 887 Van Damme, M., Clarisse, L., Whitburn, S., Hadji-Lazaro, J., Hurtmans, D., Clerbaux, C., and
888 Coheur, P.-F.: Industrial and agricultural ammonia point sources exposed, *Nature*, 564,
889 99–103, <https://doi.org/10.1038/s41586-018-0747-1>, 2018.

- 890 Vira, J., Hess, P., Ossohou, M., and Galy-Lacaux, C.: Evaluation of interactive and prescribed
891 agricultural ammonia emissions for simulating atmospheric composition in CAM-chem,
892 *Atmos. Chem. Phys.*, 22, 1883–1904, <https://doi.org/10.5194/acp-22-1883-2022>, 2022.
- 893 Wang, R., Guo, X., Pan, D., Kelly, J. T., Bash, J. O., Sun, K., Paulot, F., Clarisse, L., Van
894 Damme, M., Whitburn, S., Coheur, P.-F., Clerbaux, C., and Zondlo, M. A.: Monthly
895 patterns of ammonia over the contiguous United States at 2-km resolution, *Geophys. Res.
896 Lett.*, 48, <https://doi.org/10.1029/2020gl090579>, 2021.
- 897 Wang, R., Pan, D., Guo, X., Sun, K., Clarisse, L., Van Damme, M., Coheur, P.-F., Clerbaux,
898 C., Puchalski, M., and Zondlo, M. A.: Bridging the spatial gaps of the Ammonia Monitoring
899 Network using satellite ammonia measurements, *Atmos. Chem. Phys.*, 23, 13217–13234,
900 <https://doi.org/10.5194/acp-23-13217-2023>, 2023.
- 901 Wang, S., Nan, J., Shi, C., Fu, Q., Gao, S., Wang, D., Cui, H., Saiz-Lopez, A., and Zhou, B.:
902 Atmospheric ammonia and its impacts on regional air quality over the megacity of
903 Shanghai, China, *Sci. Rep.*, 5, 15842, <https://doi.org/10.1038/srep15842>, 2015.
- 904 Warner, J. X., Dickerson, R. R., Wei, Z., Strow, L. L., Wang, Y., and Liang, Q.: Increased
905 atmospheric ammonia over the world's major agricultural areas detected from space:
906 Global Atmospheric NH₃ 14 Year Trends, *Geophys. Res. Lett.*, 44, 2875–2884,
907 <https://doi.org/10.1002/2016GL072305>, 2017.
- 908 Zhang, L., Jacob, D. J., Knipping, E. M., Kumar, N., Munger, J. W., Carouge, C. C., van
909 Donkelaar, A., Wang, Y. X., and Chen, D.: Nitrogen deposition to the United States:
910 distribution, sources, and processes, *Atmos. Chem. Phys.*, 12, 4539–4554,
911 <https://doi.org/10.5194/acp-12-4539-2012>, 2012.
- 912 Zhang, L., Chen, Y., Zhao, Y., Henze, D. K., Zhu, L., Song, Y., Paulot, F., Liu, X., Pan, Y., Lin,
913 Y., and Huang, B.: Agricultural ammonia emissions in China: reconciling bottom-up and
914 top-down estimates, *Atmos. Chem. Phys.*, 18, 339–355, <https://doi.org/10.5194/acp-18-339-2018>, 2018.
- 916 Zhu, L., Henze, D. K., Cady-Pereira, K. E., Shephard, M. W., Luo, M., Pinder, R. W., Bash, J.
917 O., and Jeong, G.-R.: Constraining U.S. ammonia emissions using TES remote sensing
918 observations and the GEOS-Chem adjoint model: INVERSE MODELING OF
919 NH₃ EMISSIONS, *J. Geophys. Res.*, 118, 3355–3368, <https://doi.org/10.1002/jgrd.50166>,
920 2013.